INFORMATION TO USERS

This manuscript has been reproduced from the microfilm master. UMI films the text directly from the original or copy submitted. Thus, some thesis and dissertation copies are in typewriter face, while others may be from any type of computer printer.

The quality of this reproduction is dependent upon the quality of the copy submitted. Broken or indistinct print, colored or poor quality illustrations and photographs, print bleedthrough, substandard margins, and improper alignment can adversely affect reproduction.

In the unlikely event that the author did not send UMI a complete manuscript and there are missing pages, these will be noted. Also, if unauthorized copyright material had to be removed, a note will indicate the deletion.

Oversize materials (e.g., maps, drawings, charts) are reproduced by sectioning the original, beginning at the upper left-hand corner and continuing from left to right in equal sections with small overlaps. Each original is also photographed in one exposure and is included in reduced form at the back of the book.

Photographs included in the original manuscript have been reproduced xerographically in this copy. Higher quality 6" x 9" black and white photographic prints are available for any photographs or illustrations appearing in this copy for an additional charge. Contact UMI directly to order.

UMI®

Bell & Howell Information and Learning
300 North Zeeb Road, Ann Arbor, MI 48106-1346 USA
800-521-0600

Low-Jitter Symbol Timing Recovery for M-ary QAM and PAM Signals

Afshin Haghighat

A Thesis

in

The Department

of

Electrical Engineering

Presented in Partial Fulfillment of the Requirements

for the Degree of Master of Applied Science at

Concordia University

Montreal, Quebec, Canada

August 1998

ABSTRACT

Low-Jitter Symbol Timing Recovery for M-ary QAM and PAM Signals

Afshin Haghighat

Multi-level modulation techniques have recently gained a significant attention for broadband communications to support multimedia services (e.g., LMDS/LMCS, cable-modem,...). High-performance coherent multi-level demodulation requires low-phase noise carrier recovery and low-jitter symbol timing recovery. This thesis focuses on low-jitter symbol timing recovery schemes applicable to M-ary QAM and PAM signals.

Franks and Bubrowski introduced highpass *prefiltering* and symmetric bandpass *post-filtering* for *jitter-free* operation of a symbol timing recovery scheme using a squarer for *binary* signaling [5]. We show that the same conditions are also applied to M-ary PAM or QAM signals. The *jitter-free* operation requires the amplitude response of the prefilter to be precisely matched to the Fourier transform of the received signal. In addition, it assumes a prior knowledge of the symbol timing frequency in order to achieve the symmetry of the spectrum about the Nyquist frequency. These requirements are difficult to meet in practice, and hence, the effectiveness of prefiltering has been questioned [7]. In this work, we have investigated the effects of imperfections in both prefiltering and post-filtering on the jitter performance using analysis, simulation and experiments. It is shown that, although a *zero-jitter* cannot be achieved due to the imperfections, a good selection

of *pre-filtering* can significantly reduce the timing jitter of the recovered clock signal. Jitter performance of the squarer with and without prefiltering for M-ary PAM signals is presented.

We also demonstrated that a perfect *prefiltering* of the received *baseband* signal essentially produces an equivalent *double-sided band, suppressed-carrier* (DSB-SC) passband signal centered at the Nyquist frequency (i.e., ½ of the symbol clock frequency). Therefore, the *squarer* actually plays the role of a carrier recovery of the *equivalent* DSB-SC signal and reproduces a carrier tone at *twice* the Nyquist frequency. This observation leads to the introduction of a Costas-loop to replace both the *squarer* and the bandpass *post-filter*. Subsequently, we show that the required *prefiltering* can be embedded in the Costas-loop lowpass filters. In this approach, the needs for matched highpass pre-filtering and symmetric bandpass post-filtering are eliminated and a very low jitter recovered symbol clock signal can be achieved with a simple Costas loop. Jitter performance can be enhanced with a narrow lowpass loop filters. Furthermore, the introduced Costas-loop does not employ any non-linear operation, which otherwise could introduce more jitter due to the nonlinear AM-to-PM effects. Analytical and experimental results show that the introduced technique is applicable to both M-ary QAM and PAM signals to achieve a very low jitter performance without any stringent requirement.

ACKNOWLEDGMENTS

I would like to thank my thesis supervisor, Dr. Tho Le-Ngoc, for his help and support throughout different steps of the research and also, for providing variety of research tools which gave me a valuable learning opportunity.

I also would like to express my gratitude to my family, for their continuous support and encouragement.

TABLE OF CONTENTS

LIST OF FIGURES

LIST OF TABLES

LIST OF SYMBOLS

A	Constant, amplitude
$A(f)$	Local definition
a_k	Discrete random variable, data
$a(t)$	Output signal of the lowpass filter at the in-phase arm
B	Bandwidth of the $H(f)$
$B(f)$	Local Definition
BW_{3dB}	Half power bandwidth of the tuned filter
$b(t)$	Output signal of the lowpass filter at the quadrature arm
$C(f)$	Local Definition
$C_f(f)$	Fourier transform of $c(t)$
C_1	Constant, local definition
C_2	Constant, local definition
C/N	Carrier to noise ratio
$c(t)$	Filtered signal at the in-phase arm
d	Eye opening
d'	Reduced eye opening
$e(t)$	Error signal
f_c	Corner frequency of filters

f_o Symbol rate frequency

$G_\varphi(f)$ Phase-jitter spectral density function

$G_{W'}(f)$ Spectral density of the timing wave

$g(t)$ Received pulse after prefiltering

$H(f)$ Transfer function of the prefilter replacement

$J_{p\text{-}p}$ Peak to peak jitter

$J_{rms.}$ rms. jitter

K_1 Mixer conversion gain

K_2 Mixer conversion gain

$L(f)$ Transfer function of the Loop filter

$M(f)$ Transfer function of the arm filter

m Slope of raised-cosine spectrum at Nyquist frequency

n order of filters

$n(t)$ White gaussian noise

Q Quality factor of the tuned filter

$q_m(t)$ Output of the tuned filter to $z_m(t)$

$R_{W'}(\tau)$ Autocorrelation function of the timing wave

$R_\varphi(\tau)$ Autocorrelation function of the phase-jitter function

$r(t)$ Received data stream

$S_f(f)$ Fourier transform of $s(t)$

$s(t)$ Filtered signal at the quadrature arm

T_O Symbol clock period

t_O Nominal point of clock zero-crossing

t_D Delay time of the tuned filter

$u(t)$ Received pulse shape

$V(f)$ Transfer function of the tuned filter

V_r Variance terms

$v(t)$ Impulse response of the tuned filter

$w(t)$ Timing wave

$x(t)$ Received signal after prefiltering

$y(t)$ Received data stream after nonlinear transformation

$z_m(t)$ Local definition

Γ Nonlinear transformation

$\Omega(t)$ A bandlimited baseband signal

α Roll-off factor of the raised-cosine signal

η Eye reduction factor

$\varphi(t)$ Phase jitter function

λ_1 Local definition

λ_2 Local definition

μ_I Local definition

θ_e Phase error

ω_O Symbol rate frequency (angular)

$Var( )$ Variance function

$E[ ]$ Expected value function

Chapter 1

INTRODUCTION

High-level modulation schemes have recently received a great interest due to the demands of broadband communications to support multimedia services. Quadrature amplitude modulation (QAM) promises to be the key technology enabling broadband multi-media access to the home. Both new digital cable systems and wireless LMCS/LMDS (Local Multipoint Communication/Distribution System) are based on 16, 32, or 64-QAM with possible extensions to higher 128 and 256-QAM, as described in DVB-C standards [1].

A block diagram of a M-QAM demodulator is shown in Figure 1.1. Coherent detection requires both carrier and symbol clock synchronization. After the successful recovery of the carrier, any timing variation (or jitter) in sampling of the in-phase (I) and quadrature (Q) demodulated signals degrades the system performance. Such performance degradation becomes more pronounced in multi-level signals [2-4]. Hence low-jitter symbol timing recovery techniques are essential for M-QAM modulation schemes.

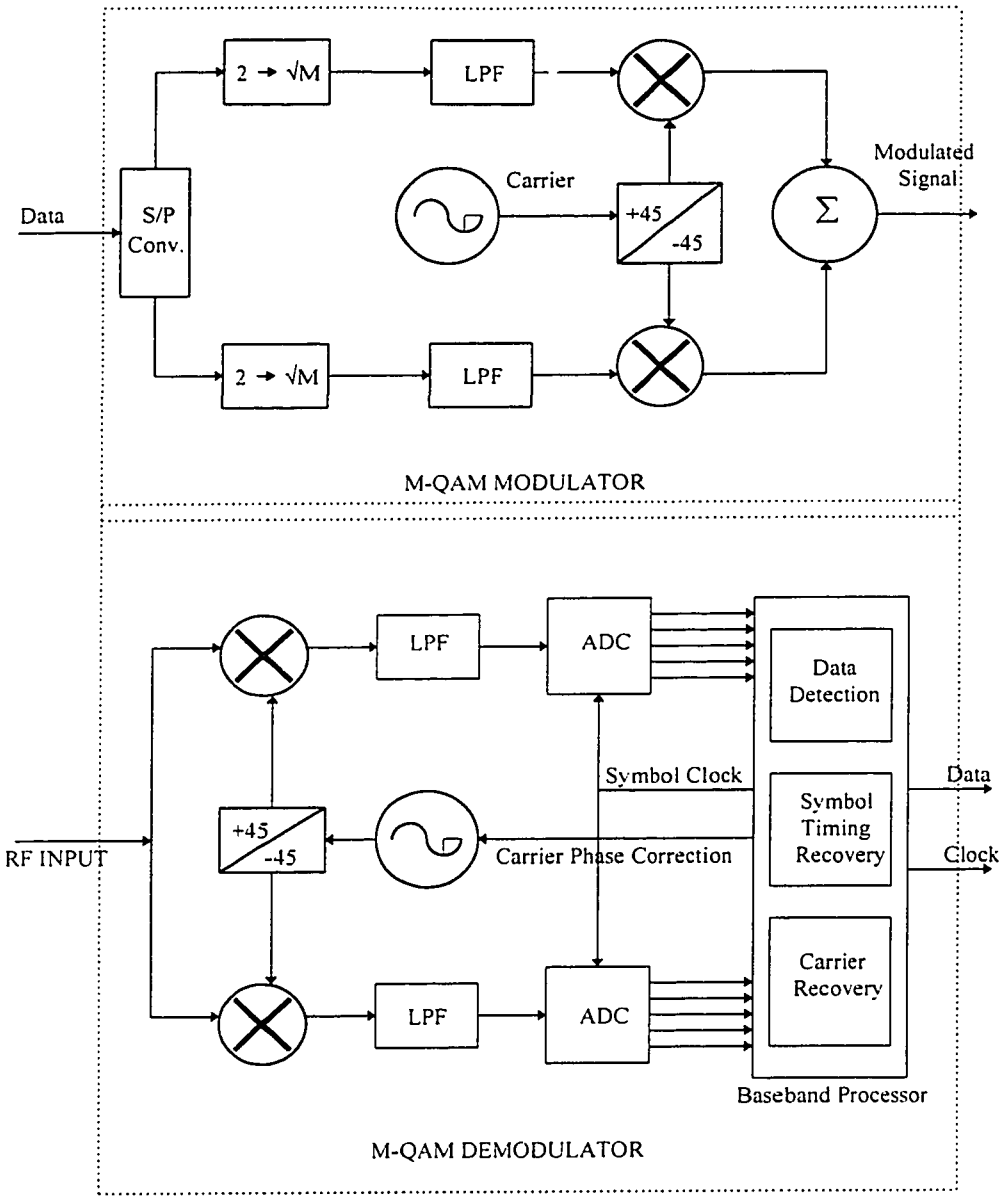

Fig. 1.1- Block diagram of a M-QAM modem

1.1) Contribution of Thesis

This thesis focuses on low-jitter STR (Symbol Timing Recovery) schemes applied to both multi-level QAM and PAM signals.

Franks and Bubrowski showed by analysis [5] that with a highpass *prefiltering* matched to the spectrum of the received baseband signal and a symmetric bandpass *post-filtering* a squarer can reproduce a *jitter-free* symbol timing clock for *binary* signaling. The *jitter-free* operation requires the amplitude response of the highpass prefilter to be precisely matched to the Fourier transform of the received signal. In addition, it assumes a prior knowledge of the symbol timing frequency in order to achieve the symmetry of the spectrum about the Nyquist frequency. These requirements are difficult to meet in practice, and hence, the effectiveness of prefiltering has been questioned [6,7]. For example, Mazo disputed the value of the proposed requirements for practical applications [6]. According to Mazo, "if the clock frequency were known exactly so that the required symmetry could be done exactly, then there would be no need to measure the clock frequency". The required conditions are not easy to meet. In practice imperfections of the prefilter and the bandpass filter cause jitter.

The first part of this research was dedicated to the study of the applicability of the above mentioned scheme to design low-jitter symbol timing recovery circuits for M-ary QAM signals. First, we extended the analysis of Franks and Bubrowski to show that the same conditions are also applied to M-ary PAM. We then investigated the effects of imperfections in both highpass *prefiltering* and bandpass *post-filtering* on the jitter performance of the squarer, and hence, assessed the effectiveness of the scheme proposed by Franks and Bubrowski. Along with analytical work, several simulations were done and a prototype was designed, implemented and tested to evaluate the jitter performance in practical conditions. Our results indicate that although the jitter-free condition cannot be achieved in practice, a good choice of a highpass prefilter can significantly improve

the jitter performance of the recovered clock signal for M-ary QAM and PAM signals.

In the second part of our research, we demonstrated that a perfect *prefiltering* of the received *baseband* signal (as proposed by Franks and Bubrowski) essentially produces an equivalent *double-sided band, suppressed-carrier* (DSB-SC) passband signal centered at the Nyquist frequency (i.e., ½ of the symbol clock frequency). Therefore, the *squarer* actually plays the role of a carrier recovery of the *equivalent* DSB-SC signal and reproduces a carrier tone at *twice* the Nyquist frequency. This observation leads to the introduction of a Costas-loop to replace both the *squarer* and the bandpass *post-filter*. Subsequently, we show that the required *prefiltering* can be embedded in the Costas-loop lowpass filters. Therefore, the Costas-loop structure *without* prefiltering can be used for zero-jitter symbol timing recovery. It is an important issue where the spectrum of the received pulse is not precisely known and prefiltering cannot be done [6]. Besides, due to its phase locked mechanism, it does not require the bandpass filter for clock extraction, the imperfection of which would have otherwise caused more jitter. In other words, the needs of matched highpass prefiltering and symmetric bandpass post-filtering are eliminated and a very low jitter recovered symbol clock signal can be achieved with a simple Costas loop. Jitter performance can be enhanced with a narrow lowpass loop filters. Furthermore, the introduced Costas-loop does not employ any non-linear operation, which otherwise could introduce more jitter due to the nonlinear AM-to-PM effects. The operation of the loop is explained and the phase detection mechanism of the loop is proved. A prototype was built and its performance was practically evaluated. Analytical and experimental results show that the introduced technique is applicable to both M-ary QAM and PAM signals to achieve a very low jitter performance without any

stringent requirement.

1.2) Organization of the Thesis

The remaining of the thesis is organized as follows.

In Chapter 2, different approaches of clock recovery are reviewed. Jitter and jitter measurement are explained and the effect of timing error in M-ary PAM and QAM is discussed.

Chapter 3 is focused on the squarer STR scheme. The jitter for an M-ary PAM is derived. Effects of imperfections in highpass pre-filtering and bandpass post-filtering are examined by both simulations and experiments.

In Chapter 4, the Costas STR architecture is introduced. The equivalence of the Costas STR and the squarer with the prefiltering is discussed. The equivalent phase detection function of the method is derived. The performance of the introduced scheme and the squarer is evaluated and compared using experiments.

In Chapter 5, after highlighting the main findings of the two preceding chapters, conclusions are summarized.

Chapter 2

SYMBOL TIMING RECOVERY

Coherent digital receivers require synchronous timing clock signals to correctly regenerate data. The receiver clock must be continuously adjusted in its frequency and phase to optimize the sampling instants of the received data signal. The timing information has to be derived from the received signal itself. In this chapter we will discuss clock recovery techniques as well as their performance requirement.

2.1) Symbol Timing Recovery Techniques

In a M-ary PAM system, digital information is carried by weighted pulses, each with identical shape and spaced uniformly by an interval T_O. A M-level baseband received signal (M-PAM) can be represented as:

$$r(t) = \sum_k a_k u(t - kT_u) + n(t) \tag{2.1}$$

where a_k is a stationary, zero mean statistically independent random variable, taking any value of $\{\pm a, \pm 3a, \pm 5a, ... \pm(M-1)a\}$, $u(t)$ represents the receiving pulse shape and $n(t)$ is

gaussian white additive noise. In band-limited systems, $u(t)$ is selected for a compact spectrum with minimum intersymbol interference (ISI) at the sampling instant. Several types of filtering are introduced to minimize frequency occupancy while controlling intersymbol interference at the sampling time. Presence of intersymbol interference during the rest of the symbol interval causes some difficulties for timing recovery process. Considering the bandwidth of systems, two families of symbol synchronizers can be distinguished: wideband and narrowband synchronizers [9].

In wideband synchronizers, bandwidth occupancy is at least equal the signaling rate. Signaling pulses are well confined to the symbol intervals. As examples of these schemes, Maximum likelihood trackers [10]-[12], Early-late gates [10], [13], [14], Transition-tracking loop [13], [15], Delay-line multiplier [16], [17] and Differentiator/crossing trigger transition detectors can be named. In the above mentioned schemes, correlators, gated integrators and transition detectors are the key elements of the design.

By emerging new applications for communication systems, it is important to exploit the frequency spectrum by employing narrowband transmission systems. In narrowband systems, bandwidth approaches the Nyquist limit of $1/2T_S$ (Hz), therefore data pulses spread and overlap over many symbol intervals. Hence, correlators and gated integrators due to pulse spreading are not applicable for data decision filters or for clock regenerator circuits. If gate time is restricted to one symbol interval, the tails of the current pulse are lost. However there will be interference from tails of neighboring pulses. If gate time spans more than one pulse interval, there is even worse interference from

other pulses. For these applications, nonlinear schemes or spectral-line schemes are used extensively [5],[8],[18],[19].

2.2) Spectral-line Schemes

Spectral-line scheme can be applied for narrowband as well as for wideband applications. Basically, in spectral-line methods, we are interested to have a discrete frequency component, containing phase and frequency information of the clock signal. Hence, by referencing to that component, we will be able to establish the timing synchronization for the link. Ironically, as shown in Figure 2.1, the spectral density of data streams, using most common pulses such as *NRZ* pulse and raised cosine signal has a null at the clock frequency [18]. By using non-band-efficient *RZ* pulse, the null at the clock frequency is eliminated, however we still do not have a proper frequency component to be referenced. In order to solve the problem, introducing a non-linear block

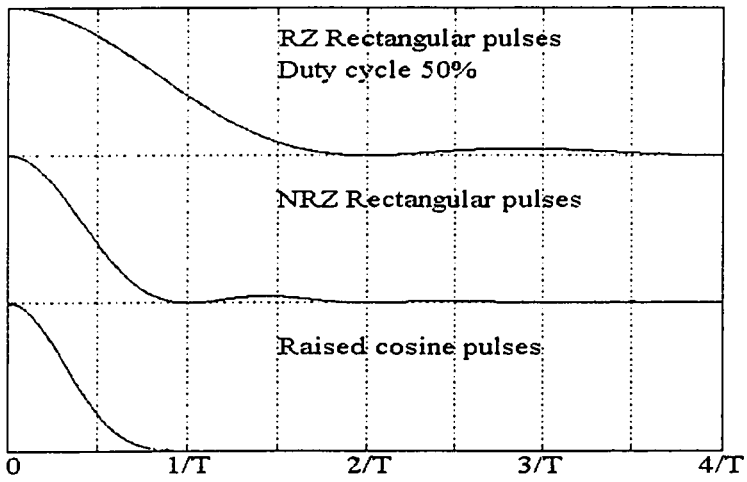

Figure 2.1- Comparison the spectrums of different signaling techniques

in the timing path is recommended. Assuming the received baseband signal $r(t)$ as in Equation (2.1) and $n(t)=0$, then $r(t)$ is a cyclostationary signal, meaning that its moments vary in time and periodic with symbol period T_O. By applying a proper non-linear transformation, signal

$$y(t) = \Gamma\{r(t)\} \tag{2.2}$$

consisting of a discrete tone at symbol rate frequency is produced. The mean value of $y(t)$ ($E[y(t)]$) unlike $r(t)$, is non-zero and periodic with period T_O. The general block diagram of the scheme is illustrated in Figure 2.2. Good examples of proper non-linearity are mostly even functions like, squarer, quadruple and rectifiers, however other solutions like delay and multiply or zero-crossing detector could be used as well [12],[17],[20],[21]. Among the first group, the squarer scheme due to having a tractable theoretical analysis as well as its performance, has been employed more than the others [5],[6],[19].

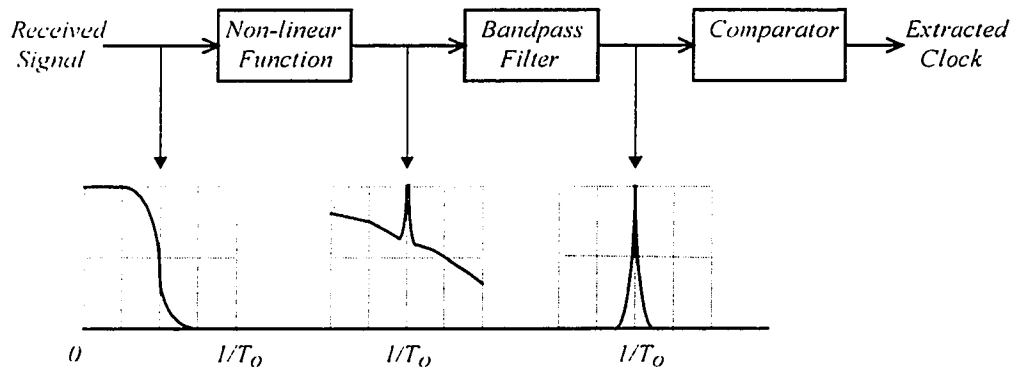

Fig. 2.2- Block diagram of Spectral-line schemes and signal spectra

2.3) Jitter in Synchronizers

The CCITT defines jitter [22] as " short term variations of the significant instants of a digital signal from their ideal positions in time" [23]. As shown in Figure 2.3, timing jitter can be considered as a form of phase noise present on the digital signal. In general, the instantaneous output of a timing recovery unit (timing wave) can be modeled as:

$$w(t) = \sqrt{2}\,ASin(\omega_{\circ}t + \varphi(t)) \tag{2.3}$$

where A is assumed constant and f_O is the symbol rate frequency and $\varphi(t)$ is the phase jitter (noise) function. Phase jitter $\varphi(t)$ modulates the phase of the timing wave $w(t)$. As a result of it, the zero crossing points of the timing wave and consequently the clock signal will be perturbed (Δt) about the nominal points (Figure 2.3). In an ideal case of zero jitter $\varphi(t)=0$, however in real life, phase jitter function $\varphi(t)$ usually represents a random process with zero mean average.

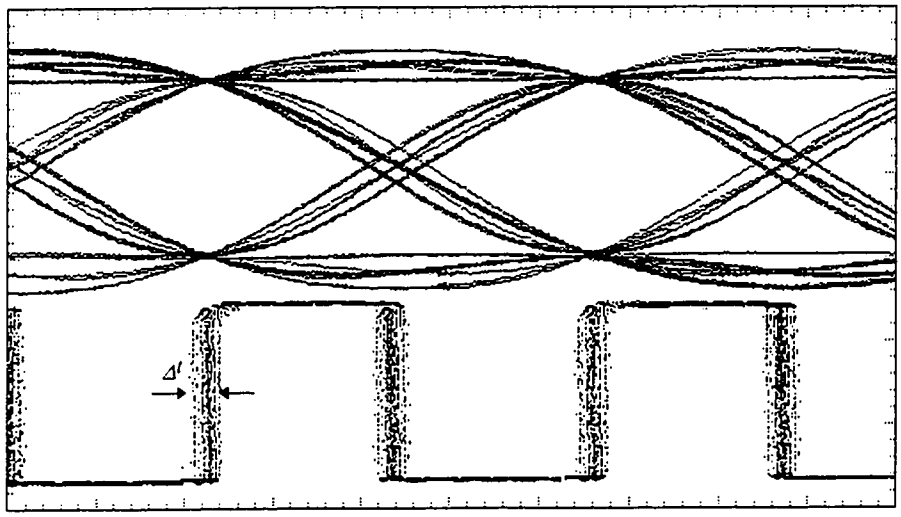

Figure 2.3- Fluctuations of clock edges about the nominal points

2.4) Phase Noise Interpretation in the Time Domain

As discussed earlier, intersymbol interference is a deciding factor in symbol timing recovery concept. As ISI grows up, due to pulse spreading in the time domain, zero-crossing points of the received signal exhibit a wide variation about the nominal point. For example, a raised-cosine signal with α=0.5 shows a peak to peak fluctuation of zero-crossing points close to 17% of the symbol interval (Figure 2.3). When such a narrowband signal, is applied to a non-linear block, variations of zero-crossing points are translated into the phase of the clock component (AM-PM effect) . In this translation, depending on the type of the nonlinearity, the phase noise can be magnified differently. Although a narrow bandpass filter can reduce the effect of the disturbances, the damage is already done. In general, the recovered clock always has a jitter component caused by ISI. However, its amount depends on the type of the employed scheme. Since the jitter is caused by the data pattern it is called pattern noise or pattern jitter.

Jitter performance can be evaluated in both time and frequency domain. In time domain, as shown in Figure 2.3, jitter can be measured as the peak to peak or rms. value of the perturbation Δt. In practice, we can observe and measure the jitter of the recovered clock by triggering an oscilloscope with a reference clock. By this approach, peak to peak $(\Delta t_{p\text{-}p})$ or rms. $(\Delta t_{rms.})$ fluctuations of the edges of the extracted clock can be measured. In this way, high amplitude perturbations that may cause cycle slipping, due to having a very low frequency of occurrence are ignored. The measured peak to peak value, does not reflect the statistical characteristics of the jitter, however it does give an efficient result for a relative measurement between different approaches.

2.5) Phase Noise Interpretation in the Frequency Domain

Figure 2.4 shows the spectral-density of the received signal after passing through a nonlinear device. As explained in the previous section, variations of zero-crossing points of the data signal due to intersymbol interference are translated into the phase of the recovered clock. In the frequency domain, this phenomenon can be demonstrated as the background noise that comes with the clock component. The shape of the background noise is a function of statistical characteristics of the data and also the employed timing recovery technique. In order to lessen the contribution of the pattern noise, narrowband bandpass filtering is required. As shown in Figure 2.4, in most applications the contribution of white noise is much less destructive than the pattern noise.

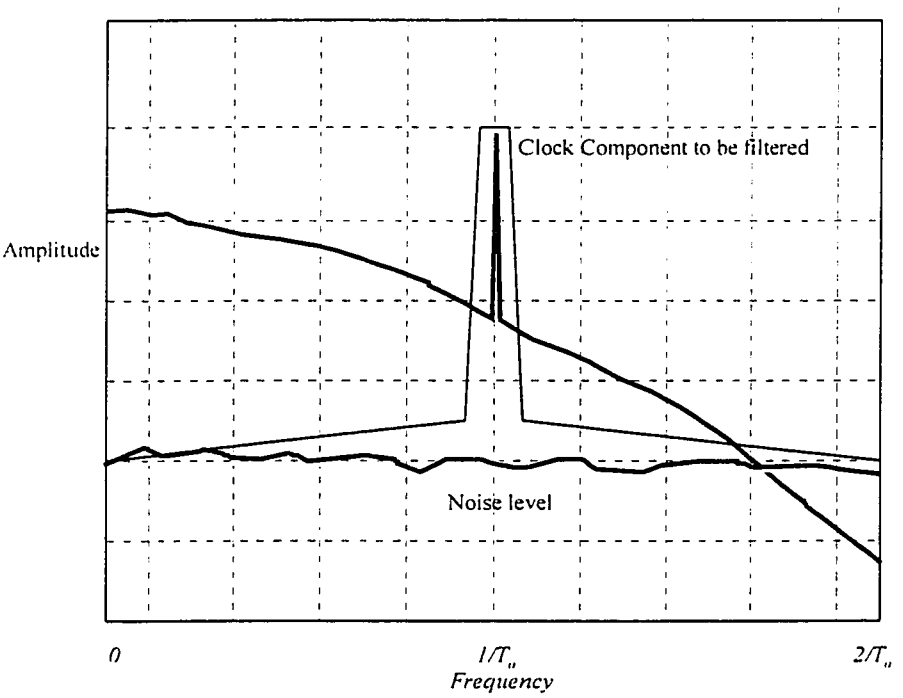

Figure. 2.4- Spectra-density of the received signal after the nonlinear block

Although jitter measurement in time domain provides jitter amplitude statistics, it does not contain information about the frequency content of the jitter. The jitter power spectrum is defined as the amount of jitter per unit frequency and is usually expressed in units of $(Degrees^2/Hz)$ [23]. A typical phase noise spectral density of the recovered clock is shown in Figure 2.5. The vertical axis represents the mean-square value of the phase noise per Hertz in terms of $(Degrees^2/Hz)$ in logarithmic scale and the horizontal axis is scaled based on the frequency offset from the clock component. Considering the mathematical representation of the timing wave as Equation (2.3), it can be expanded as follows [24], [25],

$$w(t) = \sqrt{2}ASin\omega_n tCos\varphi(t) + \sqrt{2}ACos\omega_n tSin\varphi(t) \tag{2.4}$$

Assuming that $\varphi(t)$ is a stationary random process and assuming further it has a low phase noise of $\varphi(t)$,

$$w(t) \cong \sqrt{2}ASin\omega_n t + \sqrt{2}A\varphi(t)Cos\omega_n t. \tag{2.5}$$

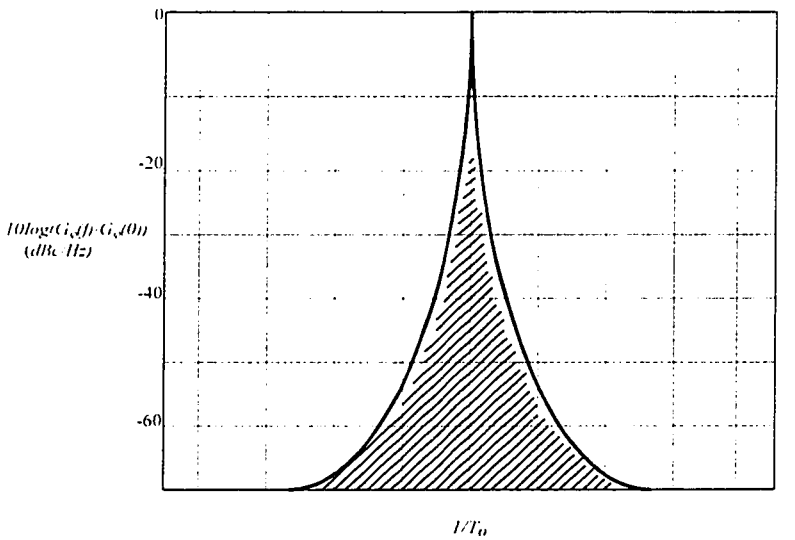

Fig. 2.5- Close view of the spectrum of the recovered clock

The autocorrelation function is given by:

$$R_w(\tau) = A^2 Cos\omega_n \tau + A^2 R_\varphi(\tau) Cos\omega_n \tau \tag{2.6}$$

where $R_\varphi(\tau)$ is the autocorrelation function of the phase jitter function. The power spectral density function of the recovered clock is given by:

$$G_w(f) = \frac{A^2}{2}\left[\delta(f + f_n) + \delta(f - f_n)\right] + \frac{A^2}{2}\left[G_\varphi(f + f_n) + G_\varphi(f - f_n)\right]. \tag{2.7}$$

where $G_W(f)$ is the spectral density function of the timing wave. For low phase noise, the spectral density of the recovered clock is indeed the shifted version of the spectral density of the phase noise function $\varphi(t)$. The root mean-square value of the jitter can be evaluated by:

$$\Delta t_{rms}^2 = \int_{-\infty}^{\infty} G_\varphi(f) df. \tag{2.8}$$

Equations (2.7) and (2.8) imply that as an alternative way of jitter measurement, we can estimate the Δt_{rms}^2 simply by integrating the area under the spectrum of the timing wave, $G_W(f)$:

$$\Delta t_{rms}^2 = \int_{0}^{\infty} G_w(f) df. \tag{2.9}$$

2.6) Jitter and Bit Error Rate Performance

Nyquist pulses are well suited for optimum data detection. Ideally, the tails of one pulse go through zero at the sampling times of all other pulses. Therefore by minimizing the intersymbol interference term, the maximum probability of correct decision is gained.

In such a circumstance, the best sampling instant is the point where benefits from the maximum eye opening. As shown in Figure 2.6, any phase offset from the best sampling point is equivalent to reducing the eye opening which means degradation in the bit error rate performance of the system. In a multi-level data transmission system, each symbol represents a group of bits. Hence, the impact of the phase error on the BER performance is obviously more significant.

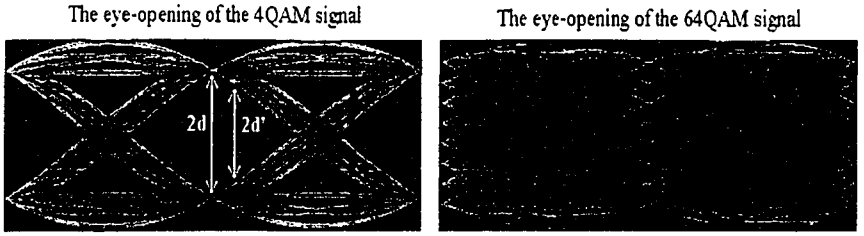

Figure 2.6- Eye-closing effect due to phase offset

As a result of eye opening reduction, the transmitter has to pump more power into the transmission medium. The effect of phase error can be translated in term of an increase in *C/N* ratio (Carrier to Noise ratio) [2]-[4]. The amount of impact of the clock phase error on *C/N*, depends on the data pattern. This matter can be more clarified by considering the fact that at any time except the maximum eye opening, an infinite number of signal levels associated with different data pattern can be expected. Due to infinite variety of patterns, it would be more instructive to consider a bound for the impact of the clock phase error on the system performance. The maximum probability of error occurs for the data sequence that gives the minimum eye opening. In Figure 2.6, d represents the amplitude of the received signal at the middle of eye opening and d' is the amplitude of the received signal at a phase off-set from the maximum opening. For this sequence, equivalent increase in *C/N* ratio due to clock phase error can be approximated as [4]:

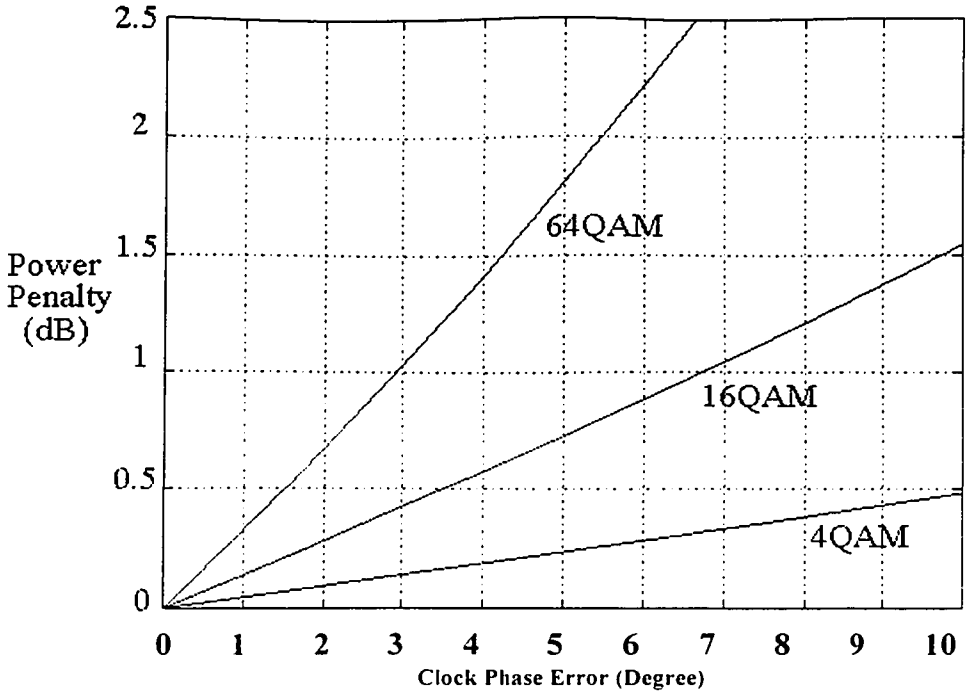

Fig. 2.7- C/N degradation due to clock phase error

$$Penalty_{C/N} = 20\log(d'/d) = 20\log(\eta) \tag{2.10}$$

where η is the amplitude reduction factor for a particular phase error. In Figure 2.7, the *C/N* degradation for different values of phase error is shown. From Figure 2.7, it can be noted that for 64-QAM, a clock phase error of only 3° leads to 1dB degradation in *C/N* (worst case). Although the result presented in Figure 2.7, is basically found for a case of static phase error, it can be used to depict the worst case for a system, which has certain amount of peak to peak jitter. Besides, by having this result and averaging over the probability distribution function of the jitter function of a known system, average power penalty can be obtained.

Chapter 3

SQUARER TIMING SYNCHRONIZER

Prefiltering is recommended for jitter-free operation of the squarer timing recovery. Franks and Bubrowski [5] proved that for a 2-level PAM transmission, the squarer scheme with prefiltering can achieve a jitter-free performance if certain symmetry and bandlimiting conditions are imposed on the spectrum of the prefiltered signal $G(f)$ and frequency response of the bandpass filter $V(f)$.

In this chapter, jitter term for a general M-level PAM is derived similar to the procedure presented in [5]. It is shown that the same set of conditions as 2-level PAM are required for jitter-free operation. Since it is quite difficult to design a prefilter and a bandpass filter to comply with the requirements, the impact of imperfection is investigated. It is shown that the Butterworth prefilter can significantly improve jitter performance of the squarer STR.

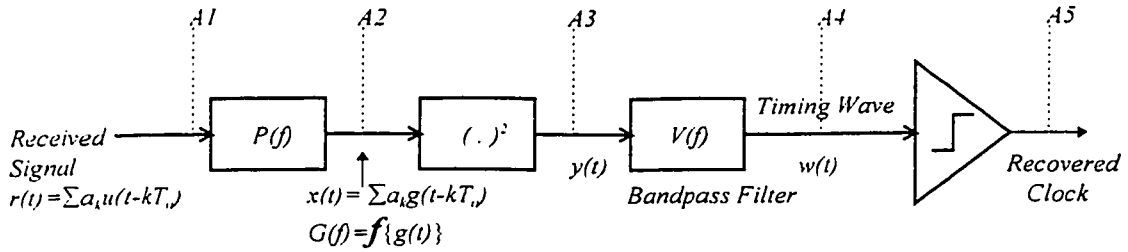

Figure 3.1- Squarer Timing Recovery

3.1) Squarer Symbol Timing Recovery

The block diagram of the squarer STR with prefiltering is shown in Figure 3.1. It consists of a prefilter, a squarer circuit, a bandpass filter and a comparator. Figure 3.2 shows the signals at the different points (A1-A5) of the circuit. Trace A1 in Figure 3.2 shows the received signal. The received signal *r(t)* as defined in Equation (2.1) is passed through the prefilter. It is assumed that the additive noise *n(t)* is not present. The prefilter reshapes the received signal to have a symmetric spectrum about the Nyquist frequency $1/2T_O$. The signal at the prefilter output can be represented as

$$x(t) = \sum_k a_k g(t - kT_o), \tag{3.1.a}$$

$$g(t) = u(t) * p(t), \tag{3.1.b}$$

where *p(t)* is the impulse response of the prefilter. Prefiltered signal A2 in Figure 3.2, is similar to a DSB-SC signal, modulated at a carrier frequency of $1/2T_O$. This signal is fed to the squarer. The squared signal *y(t)* shown in trace A3, can be represented as

$$y(t) = \left(x(t)\right)^2 = \left(\sum_k a_k g(t - kT_o)\right)^2 = \sum_m \sum_k a_k a_{k+m} z_m (t - kT_o) \tag{3.2}$$

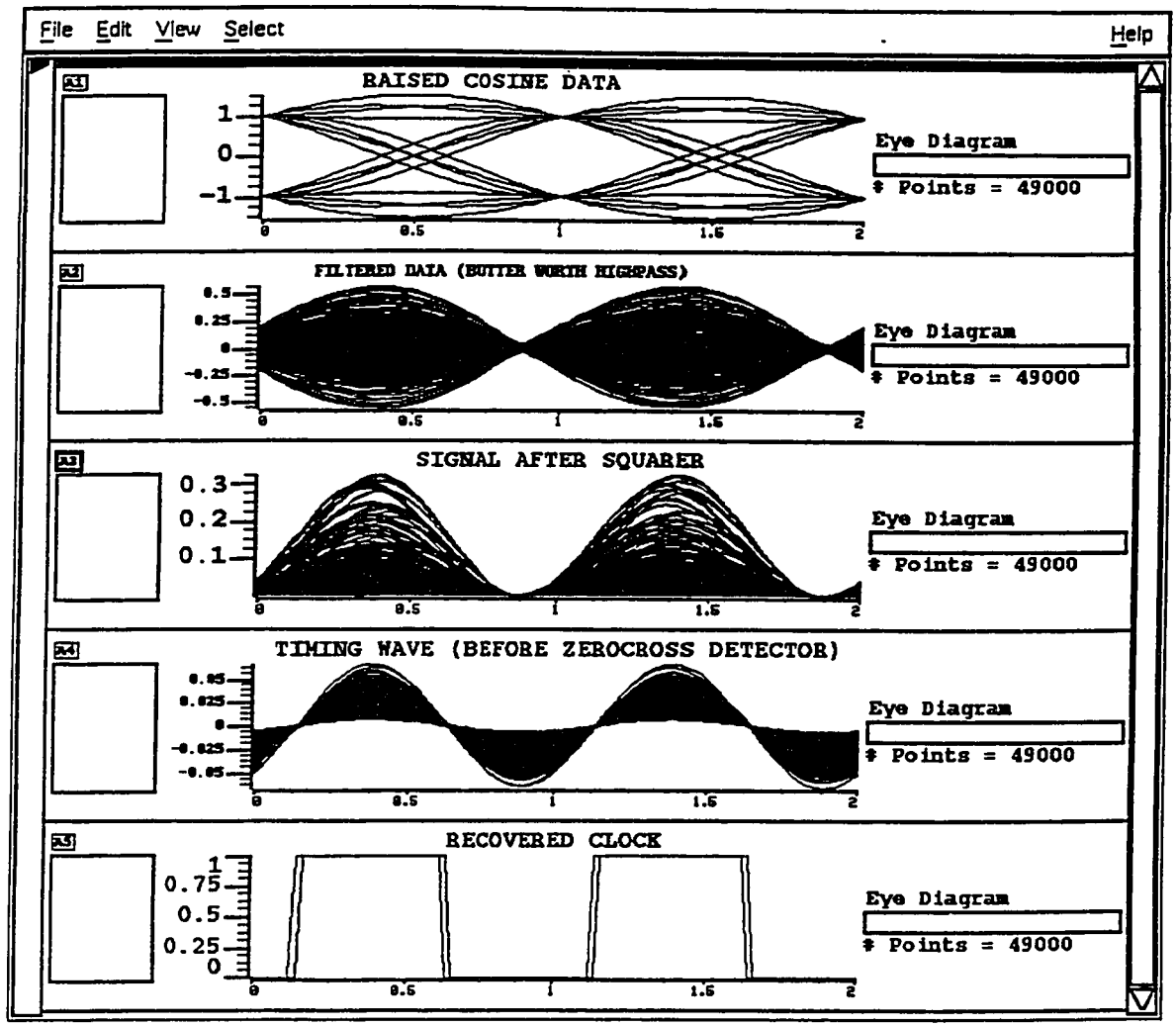

Figure 3.2- Signals at different points of the squarer timing recovery circuit

where $z_m(t)=g(t)g(t-mT_o)$. To have a better understanding of the process, Equation(3.2) can be sorted as follows.

$$y(t) = (x(t))^2 = \left(\sum_k a_k g(t - kT_o) \right)^2$$
$$= \sum_k a_k^2 g^2(t - kT_o) + \sum_{n,m}^{n \neq m} a_n a_m g(t - nT_o) g(t - mT_o). \quad (3.3)$$

The signal $y(t)$ consists of two terms. The first summation represents harmonic component, and the second creates a background or pattern noise. As shown in Figure 3.2, the signal at point A3 has a periodic component at clock frequency that is related to the first term in Equation(3.3). The bandpass filter $V(f)$ extracts the tone component to produce the timing wave $w(t)$ at point A4. From Equation (3.2),

$$w(t) = y(t) * v(t) = \left(\sum_m \sum_k a_k a_{k+m} z_m(t - kT_o) \right) * v(t)$$
$$= \sum_m \sum_k a_k a_{k+m} q_m(t - kT_o) \quad (3.4)$$

where $q_m(t)=z_m(t)*v(t)$ and $v(t)$ is the impulse response of the bandpass filter. The comparator detects zero crossings of the timing wave and regenerates the clock signal, point A5.

3.2) Jitter Analysis of the Squarer Timing Recovery

Figure 3.3.a shows a typical form of the timing signal $w(t)$. To evaluate the jitter, behavior of the timing wave $w(t)$ must be investigated. Jitter is defined as the ratio of fluctuation of the zero-crossing points of the timing wave about the nominal point t_O, to the period of the clock.

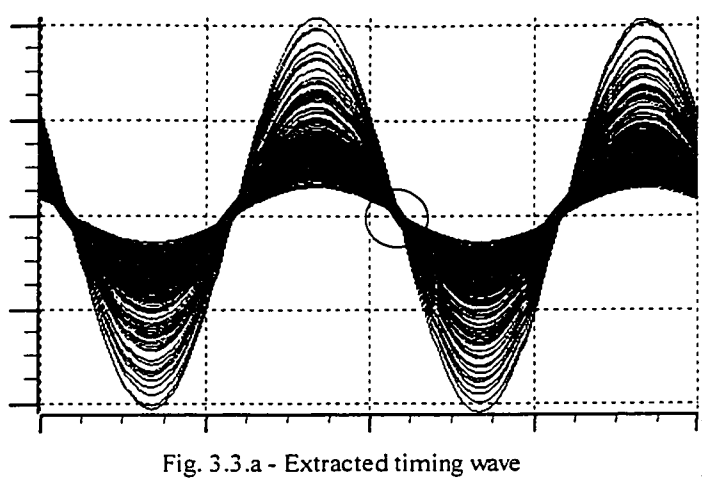

Fig. 3.3.a - Extracted timing wave

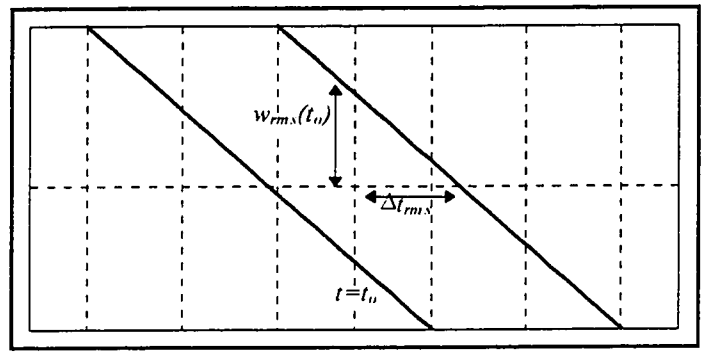

Figure 3.3.b- Linear extrapolation of zero-crossing points of the timing wave

$$J_{rms} = \frac{\Delta t_{rms}}{T_o}. \tag{3.5}$$

Evaluating Δt_{rms} based on actual zero-crossing points of the timing wave is difficult. An appropriate approximation can be obtained by locating the zero-crossings of the $w(t)$ by linear extrapolation using the mean slope of the timing wave at the mean zero crossing [5]. Hence, the fluctuation of Δt_{rms} as shown by a simple geometry in Figure 3.3.b can be evaluated by the ratio of the root mean-squared value of the timing wave to the average value of the slope of the timing wave at the nominal zero-crossing point, t_o.

$$\Delta t_{rms} = \left| \frac{\sqrt{E\left[w(t)^2\right]}}{\frac{d}{dt} E\left[w(t)\right]} \right|_{t=t_0} \tag{3.6}$$

Since the $\{a_k\}$ represents a statistically independent stationary sequence,

$$\begin{aligned} E\left[w(t)\right] &= \sum_m \sum_k E\left[a_k a_{k+m}\right] q_m(t - kT_0) \\ &= E\left[a^2\right] \sum_k q_0(t - kT_0). \end{aligned} \tag{3.7}$$

By using Poisson sum formula Equation (3.7) can be re-written as:

$$E\left[w(t)\right] = \frac{E\left[a^2\right]}{T_0} \sum_l V\left(\frac{l}{T_0}\right) Z_0\left(\frac{l}{T_0}\right) \exp\left(\frac{j2\pi lt}{T_0}\right). \tag{3.8}$$

$V(f)$ represents the transfer function of a narrow band bandpass filter, which is centered at $1/T_0$. It can be assumed that,

$$V(l / T_0) = 0 \qquad l \neq \pm 1. \tag{3.9}$$

Equation (3.8) can be simplified as:

$$E[w(t)] = 2E[a^2]\left|\mu_1\right| Cos\left(\frac{2\pi t}{T_0} + \theta_{\mu 1}\right) \tag{3.10.a}$$

$$\mu_1 = \left|\mu_1\right| \angle \theta_{\mu 1} = \frac{1}{T_0} V\left(\frac{1}{T_0}\right) \int_{-\infty}^{+\infty} C(f) df \tag{3.10.b}$$

where,

$$C(f) = G(f) G\left(\frac{1}{T_0} - f\right). \tag{3.10.c}$$

Mean slope of the timing wave at t_0 can be derived as:

$$\frac{d}{dt}\left(E\left[w(t)\right]\right) = \frac{d}{dt}\left(2E[a^2]\left|\mu_1\right| Cos\left(\frac{2\pi t}{T_0} + \theta_{\mu 1}\right)\right). \tag{3.11}$$

At zero-crossing point t_0 we have $\frac{t_n}{T_n} = \frac{n}{4} - \frac{\theta_{\mu 1}}{2\pi}$, where n is any odd integer. Therefore,

$$\left|\frac{d}{dt}\left(E[w(t)]\right)\right|_{t=t_n} = \frac{4\pi E[a^2]|\mu_1|}{T_n}. \tag{3.12}$$

The mean-squared value of the timing wave can be defined as:

$$E[w(t)^2] = \sum_k \sum_m \sum_j \sum_l E[a_k a_{k+m} a_{k+j} a_{k+j+l}]\, q_m(t - kT_n) q_l(t - kT_n - jT_n), \tag{3.13}$$

$$E[a_k a_{k+m} a_{k+j} a_{k+j+l}] = \begin{cases} E[a^4] & \text{if} \quad m = l = j = 0 \\ E[a^2]^2 & \text{if} \quad m = l = 0,\ j \neq 0 \\ & \text{if} \quad m = j \neq 0,\ l = -j \\ & \text{if} \quad m = l \neq 0,\ j = 0 \\ 0 & \text{otherwise.} \end{cases} \tag{3.14}$$

Using Equation (3.14) in Equation (3.13), we have:

$$E[w(t)^2] = \left\{E[a^2]\sum_k q_0(t - kT_n)\right\}^2 + \left(E[a^4] - 3E[a^2]^2\right)\sum_k q_0^2(t - kT_n) + E[a^2]\sum_k \sum_m q_m(t - kT_n) q_{-m}(t - kT_n - mT_n) + E[a^2]\sum_k \sum_m q_m^2(t - kT_n) \tag{3.15}$$

By referring to Equation (3.7), the first term in the above expression is equal to the square of *E[w(t)]*. Also, it can be noted that the last two terms are equivalent. Equation (3.15) can be re-written as:

$$E[w(t)^2] = \left(E[w(t)]\right)^2 + \left(E[a^4] - 3E[a^2]^2\right)\sum_k q_0^2(t - kT_n) + 2E[a^2]^2 \sum_k \sum_m q_m^2(t - kT_n) \tag{3.16}$$

Assuming that the timing wave has a zero mean at the nominal zero-crossing point, the first term in Equation (3.15) can be ignored.

$$E\left[w(t_o)^2\right] = \left(2E\left[a^2\right]^2 \sum_k \sum_m q_m^2(t - kT_o) + \left(E\left[a^4\right] - 3E\left[a^2\right]^2\right) \sum_k q_0^2(t - kT_o)\right)\Bigg|_{t=t_o} \quad (3.17)$$

By applying the Poisson formula,

$$\sum_k \sum_m q_m^2(t - kT_o) = \frac{1}{T_o} \sum_r A\left(\frac{r}{T_o}\right) \exp\left(j\frac{2\pi rt}{T_o}\right), \quad (3.18.a)$$

$$\sum_k q_0^2(t - kT_o) = \frac{1}{T_o} \sum_r B\left(\frac{r}{T_o}\right) \exp\left(j\frac{2\pi rt}{T_o}\right) \quad (3.18.b)$$

where,

$$A(f) = \sum_m \left[Q_m(f) * Q_m(f)\right] \quad (3.19.a)$$

$$B(f) = \left[Q_0(f) * Q_0(f)\right] \quad (3.19.b)$$

$$Q_m(f) = V(f) \int_{-\infty}^{+\infty} G(f - v)G(v) \exp\left(-j2\pi mT_o v\right) dv. \quad (3.19.c)$$

after some algebraic operations, $A(f)$ can be simplified to

$$A(f) = \frac{1}{T_o} \sum_l \iint H(f - v)H(v)G(f - v - \eta)G(\eta)G(v + \eta - \frac{l}{T_o})G(\frac{l}{T_o} - \eta) dv d\eta. \quad (3.20)$$

Equation (3.17) can be re-written as:

$$E\left[w(t_o)^2\right] = \sum_r V_r \exp\left(j\frac{2\pi rt}{T_o}\right)\Bigg|_{t=t_o} \quad (3.21.a)$$

$$V_r = \frac{2E\left[a^2\right]^2}{T_o} A\left(\frac{r}{T_o}\right) + \frac{E\left[a^4\right] - 3E\left[a^2\right]^2}{T_o} B\left(\frac{r}{T_o}\right). \quad (3.21.b)$$

Band-limiting Assumptions for $G(f)$ and $V(f)$:

- For high bandwidth efficiency, the bandwidth of the employed transmitted pulses are confined to at most twice the Nyquist frequency,

$$G(f) = 0 \qquad \text{for} \qquad |f| > 1/T_u . \tag{3.22}$$

By inspecting Equation (3.20), each V_r in Equation (3.21.a) has to be evaluated only for three terms corresponding to $l=0$ and $l=\pm 1$.

- $V(f)$ is a narrow-band bandpass filter satisfying,

$$V(f) = 0 \qquad \text{for} \qquad \left| |f| - 1/T_u \right| > 1/2T_u . \tag{3.23}$$

Therefore, both $A(f)$and $B(f)$ are bandlimited as $V(f)$, and V_r can be evaluated only for $r=0,\pm 2$.

As a result of these assumptions, Equation (3.21.a) can be simplified [5],

$$E\left[w(t_u)^2\right] = V_u - 2|V_2|. \tag{3.24}$$

By substituting Equation (3.12) and Equation (3.24) in Equation (3.6),

$$\Delta t_{rms} = \left| \frac{\sqrt{E\left[w(t)^2\right]}}{\frac{d}{dt} E\left[w(t)\right]} \right|_{t=t_u} = T_u \frac{\sqrt{V_u - 2|V_2|}}{4\pi E[a^2]|\mu_1|} \tag{3.25}$$

From Equation(3.21.b), terms V_0 and V_2 can be evaluated as follows:

$$V_0 = \int_{-\infty}^{+\infty} |V(f)|^2 \left\{ \frac{C_1}{T_u} \int_{-\infty}^{+\infty} |G(f+\nu)|^2 |G(\nu)|^2 d\nu \right.$$
$$\left. + 2\frac{C_1}{T_u} \mathrm{Re} \int_{-\infty}^{+\infty} C^*(f+\nu) C(\nu) d\nu + C_2 \left| \int_{-\infty}^{+\infty} G(f-\nu) G(\nu) d\nu \right|^2 \right\} df, \tag{3.26.a}$$

$$V_2 = \int_{-\infty}^{+\infty} V\left(\frac{2}{T_u} - f\right) V(f) \left\{ \frac{C_1}{T_u} \int_{-\infty}^{+\infty} C\left(f - \frac{1}{T_u} + \nu\right) C(\nu) d\nu + C_2 Z_0\left(\frac{2}{T_u} - f\right) Z_0(f) \right\} df, \tag{3.26.b}$$

where,

$$C_1 = \frac{2E[a^2]^2}{T_o}, \tag{3.27.a}$$

$$C_2 = \frac{E[a^4] - 3E[a^2]^2}{T_o}. \tag{3.27.b}$$

By using Equation(3.5),

$$J_{rms} = \frac{\Delta t_{rms}}{T_o} = \frac{\sqrt{V_o - 2|V_2|}}{4\pi E[a^2]|\mu_1|}. \tag{3.28}$$

From Equation (3.28), it is seen that the jitter is a function of statistical behavior of the input data, spectra of the prefiltered pulse *G(f)*, and frequency response of the bandpass filter *V(f)*. Franks & Bubrowski [5] proved that under certain conditions, $V_o - 2|V_2| = 0$ and jitter free operation can be achieved.

Requirements for zero jitter:

1. Fourier transform of output pulse of prefilter *G(f)* has to be a symmetric spectrum about $1/2T_O$, with a bandwidth of $1/2T_O$,

$$G(f) = \begin{cases} 0 & \Delta f_G \geq 1/4T_o \\ G(-1/2T_o + \Delta f_G) & \Delta f_G \leq 1/4T_o. \\ \text{where} \quad \Delta f_G = \left| |f| - 1/2T_o \right| \end{cases} \tag{3.29}$$

2. besides of the band limiting constraint imposed before, has to have a symmetric frequency response about the tuned frequency $1/T_O$,

$$V(f) = \begin{cases} 0 & \Delta f_V \geq 1/2T_o \\ V(-1/T_o + \Delta f_V) & \Delta f_V \leq 1/2T_o. \\ \text{where} \quad \Delta f_V = \left| |f| - 1/T_o \right| \end{cases} \tag{3.30}$$

Under these conditions, the second term in Equation(3.26.a) equals zero and for the other terms we have,

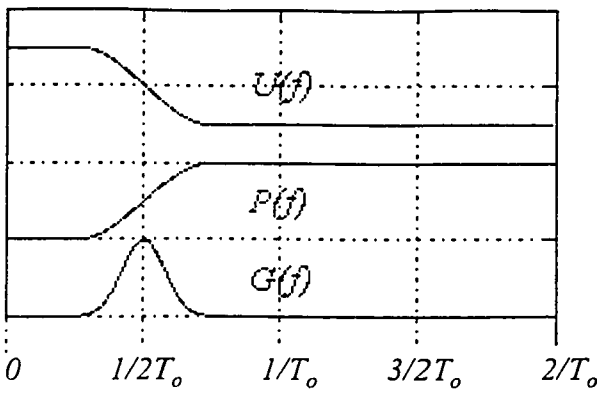

Figure 3.4- Prefiltering for zero-jitter operation

$$\frac{C_1}{T_o}\int_{-\infty}^{+\infty}|V(f)|^2\int_{-\infty}^{+\infty}|G(f+\nu)|^2|G(\nu)|^2\,d\nu df = 2\frac{C_1}{T_o}\int_{-\infty}^{+\infty}V(\frac{2}{T_o}-f)V(f)\int_{-\infty}^{+\infty}C(f-\frac{1}{T_o}+\nu)C(\nu)d\nu df, \tag{3.31.a}$$

$$C_2\int_{-\infty}^{+\infty}|V(f)|^2\left|\int_{-\infty}^{+\infty}G(f-\nu)G(\nu)d\nu\right|^2 df = 2C_2\int_{-\infty}^{+\infty}V(\frac{2}{T_o}-f)V(f)Z_0(\frac{2}{T_o}-f)Z_0(f)df. \tag{3.31.b}$$

Therefore,

$$V_o = 2|V_2|. \tag{3.31.c}$$

Figure 3.4 shows an example of prefiltering for zero jitter timing recovery. *U(f)* is the spectrum of the received signal which has a raised-cosine spectrum with α=0.5. *P(f)* is the frequency response of the prefilter and *G(f)* is the spectrum of the prefiltered signal. Since the received signal has a lowpass spectra, bandlimited to $0.75/T_O$, the prefilter is considered as a highpass filter. This highpass filter has to match to the spectrum of the received signal to produce *G(f)* with perfect symmetry about the $1/2T_O$. In practice, it is very difficult to design a prefilter perfectly matched to the spectrum of the received signal. The resulting imperfections cause jitter.

Requirements for the bandpass filter can be divided to bandlimiting and symmetry characteristics. In practice, the bandpass filter always has a bandwidth much less than the maximum value specified by the zero jitter requirements. However, the symmetry requirement is the more difficult issue for the bandpass filter design. Employing high "Q" (Quality factor) filters helps to improve the jitter performance, but the timing recovery unit will be more sensitive to mistuning and slower to recover the clock signal.

3.3) Computer Simulations

In the analysis of the squarer timing recovery scheme, there are three main issues to be analyzed based on which the system can be defined. They are:

- Transmission Bandwidth: The transmission bandwidth can be reflected in $U(f)$. As will be discussed, the transmission bandwidth can affect the type of prefilter and even, it can determine applicability of this scheme.
- Prefilter $P(f)$: For a given pulse shape, $P(f)$ has to be designed to meet the requirement in Equation (3.29). Since the requirement is not easy to meet, the impact of employing other filters has to be investigated.
- Bandpass filter $V(f)$: The bandpass filter $V(f)$ has to comply with the requirement in Equation (3.30). Although a high Q filter resembles a perfect symmetric filter for most of applications, it is quite important to relax Q requirement of the design to gain short recovery time and less complicated design.

The block diagram of the simulation model is shown in Figure 3.5. All the simulations presented in this section rely on the following hypotheses:

- **Signal source:** Multi-level PAM with root square raised-cosine filtering with roll-off factor α and a sampling frequency of 200.
- **Noise source:** Additive white Gaussian noise with one-sided power spectral density of N_0 (W/Hz).
- **Receiver filter:** Root square raised-cosine filtering with roll-off factor α.
- **Prefilter:** A highpass filter that will be explained in more details through the simulations. It is defined by the type, the order n and the cut-off frequency f_C.
- **Squarer:** It is defined by a multiplier block that multiplies the signal by itself.
- **Bandpass filter:** It is defined by the type and the Q factor.
- **Jitter measurement:** To evaluate this quantity with adequate statistical confidence, one million samples for each measurement is considered.

In each simulation, the subject is examined for three cases of 2-PAM, 4-PAM and 8-PAM except for one case (Sec. 3.3.3), in which the result of 2-PAM is equivalently applicable for the whole M-PAM family.

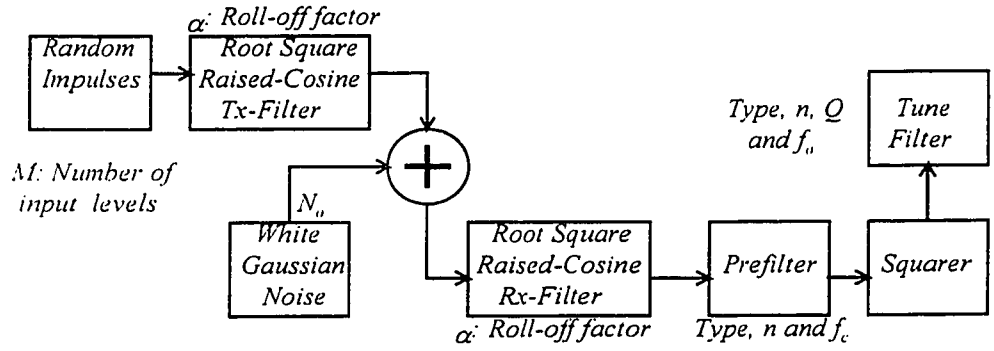

Figure 3.5- Block diagram of the simulated system

3.3.1) Transmission Bandwidth

In this simulation, the prefilter is considered as a highpass filter which has a frequency response equivalent to the reverse spectrum (mirror symmetry about $1/2T_o$) of the transmitted raised-cosine pulse. Thereby, the spectrum of the reshaped received pulse will be perfectly symmetric about the Nyquist frequency. On the other hand, the tuned filter is considered to have a rectangular shape frequency response with a $Q=1$. In such a scenario as shown in Figure 3.6, as long as the roll-off factor of the raised-cosine signal is kept under 0.5, the resulting spectrum of the shaped pulse will be bandlimited to $1/4T_O \leq f \leq 3/4T_O$, and consequently, the jitter will be zero. This behavior shows that, if the roll-off

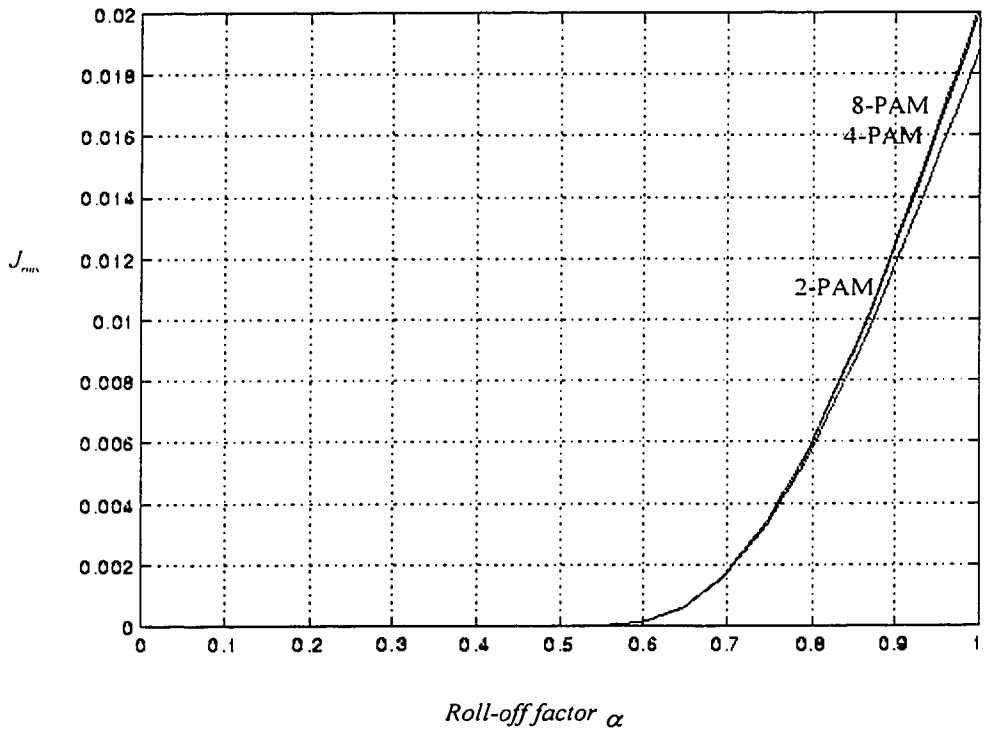

Figure 3.6- Jitter versus roll-off factor with ideal prefilter

factor exceeds 0.5 the prefilter design has to be implemented as a combination of a highpass and a bandpass filter.

In this simulation, it was assumed that α can be reduced to very low values. By referring to Equation (3.3), the power of the periodic term can be evaluated as

$$E[a^2]^2 \int_{-\infty}^{+\infty} G(f)G(1/T_n - f)df, \tag{3.24}$$

which implies that for very low values of α, the tone power will be negligible and the squarer technique cannot be applied. In practice, for low values of α higher order non-linearities such as quadruple is recommended [7].

3.3.2) Bandpass Filter

In practice, the bandpass filters with a high Q is preferred. The simulations conducted in the previous sections aimed a low value of Q (as low as one). In this section, the Q of the tuned filter is increased to ten and the same set of simulations repeated (Figure 3.7). As demonstrated, the results for different level of modulation are so close which can not be distinguished with the shown scale. By increasing the Q to ten, jitter (for α>0.5), has reduced by an order of 10^4. In fact the jitter is so low which can be ignored. In this simulation and the one presented in 3.3.1, it is assumed that the tuned filter has a symmetric frequency response with an ideal rectangular shape, which is far away from practice. At the second step of the simulation, the tuned filter has been replaced with a single tuned, 2nd order filter (RLC series) with a Q of 10. As seen in Figure 3.8, unlike the previous case in Figure 3.7, the system always has jitter

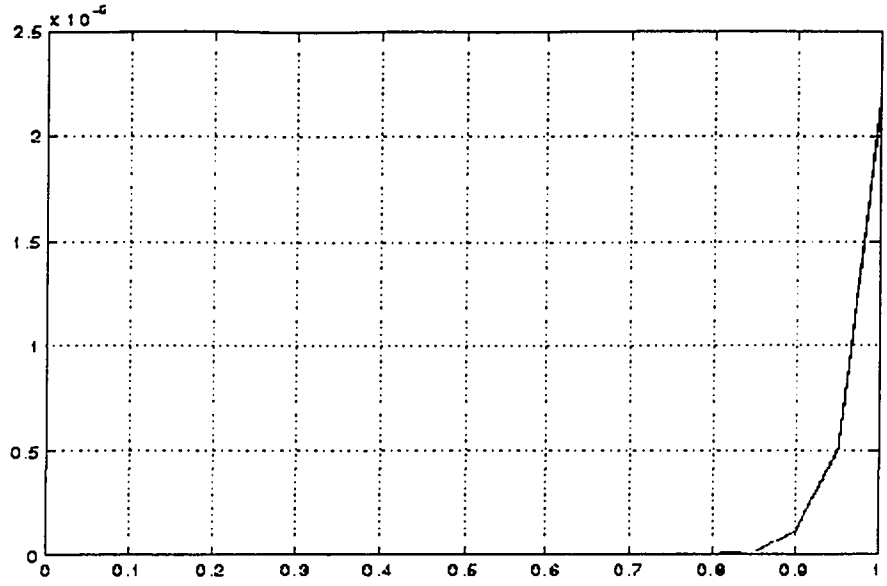

J_{rms}

Roll-off factor α

Figure 3.7 - Jitter versus α , (Rectangular *V(f), Q=10*)

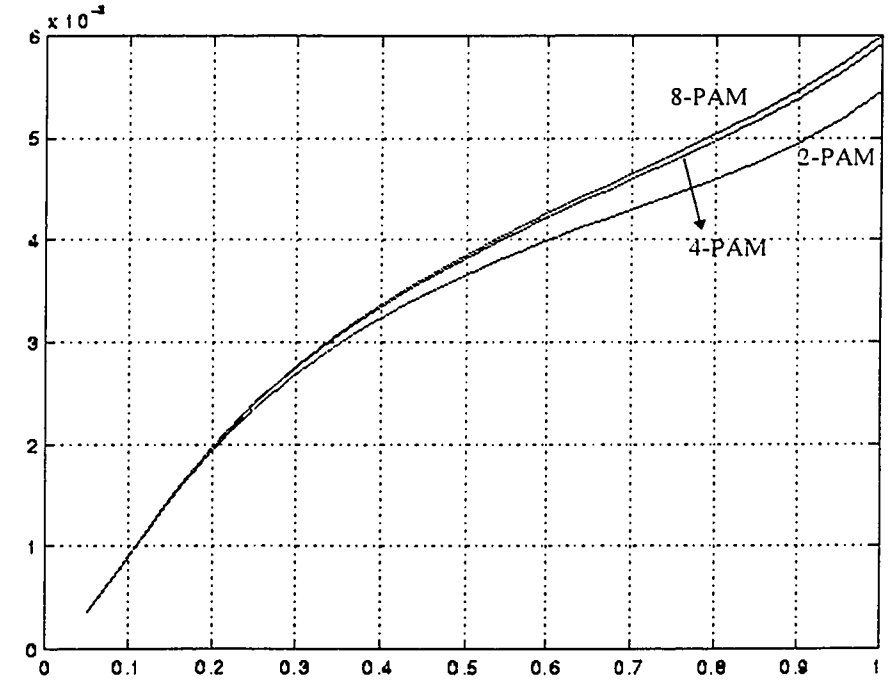

J_{rms}

Roll-off factor α

Figure 3.8- Jitter versus α, (RLC *V(f), Q=10*)

independent of the value of α. From Figure 3.6-3.8, it is observed that with increase in Q jitter is reduced. The importance of Q is more appreciated when the prefiltering is imperfect. The second noteworthy point is that, although in the case of Figure 3.8 the Q of the tuned filter is ten times higher than the case of Figure 3.6, jitter performance is worse. This behavior can essentially be addressed to the symmetry property of the tuned filter. In other words, a low Q, but symmetric bandpass filter, is preferable to a high Q, unsymmetric one.

3.3.3) Butterworth Prefiltering

So far, an ideal prefilter with a frequency response, perfectly matched to the spectrum of the raised-cosine signal was considered. In practice, a prefilter close to the desired response must be designed. As the first step, a proper type for the prefilter must be chosen. By a review on classic filters, Chebyshev or elliptic filters (due to having ripples and abrupt transition band) can lead to an unacceptable result. On the other hand Butterworth or Bessel filters may offer a satisfactory performance due to their monotonic frequency response. Comparing to Butterworth design, for a given corner frequency, the Bessel design due to its slow transition band, requires a higher order of the filter that results in a more complex and sensitive design. From the above, it is believed that the Butterworth design may be the best candidate for the prefilter. Nevertheless, it does not mean the Butterworth design offers the absolute optimum prefiltering.

Jitter is evaluated for different values of the order and the cut-off frequency of the prefilter to determine the optimum n and f_c. The analysis is done for two different values of $\alpha=0.5$ and $\alpha=0.1$ while employing a RLC tuned filter with a $Q=28$.

As illustrated in Figure 3.9 and Figure 3.10, with increase in the order of the filter, jitter performance improves. However from a certain point, relative symmetry of $G(f)$ deteriorates and jitter grows up. For both cases the best point for adjusting the cut-off frequency is a point which shows the less sensitivity of jitter to the cut-off frequency. In spite of the mentioned fact, it is seen from Figure 3.9 and Figure 3.10, that reducing the roll-off factor increases the order of the prefilter - hence the complexity. Based on the two plots, the optimum prefilters for $\alpha=0.5$ and $\alpha=0.1$ should have a cut-off frequency of $1/T_o$ with an order of $n=3$ and $n=18$ respectively.

In Figure 3.11, for a raised cosine signal with a value of $\alpha=0.5$, the symmetry of the frequency response of the prefiltered pulse for different orders of Butterworth prefilter is demonstrated (in each case corner frequency is set to the symbol rate). Based on this graphical presentation, by increasing the order of the prefilter, the spectrum is gradually shifted to the right. With an order of $n=3$, (consistent to previous result) maximum relative symmetry (that is equivalent to less jitter) is achieved.

While employing the Butterworth prefilter, zero-jitter performance can not be achieved. However, it would be instructive to know how much improvement can be gained by adding that extra hardware. In Table 3.1, the jitter value for three cases of: ideal prefiltering, no prefiltering and Butterworth prefiltering are shown. In all cases the tuned

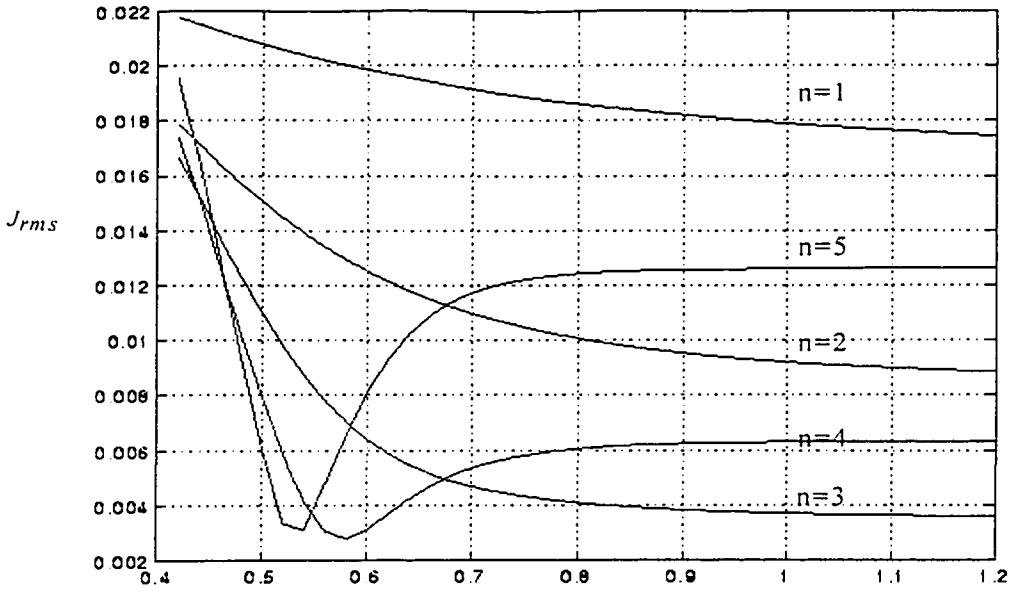

Figure 3.9 - Jitter evaluation with Butterworth filtering, (α=0.5)

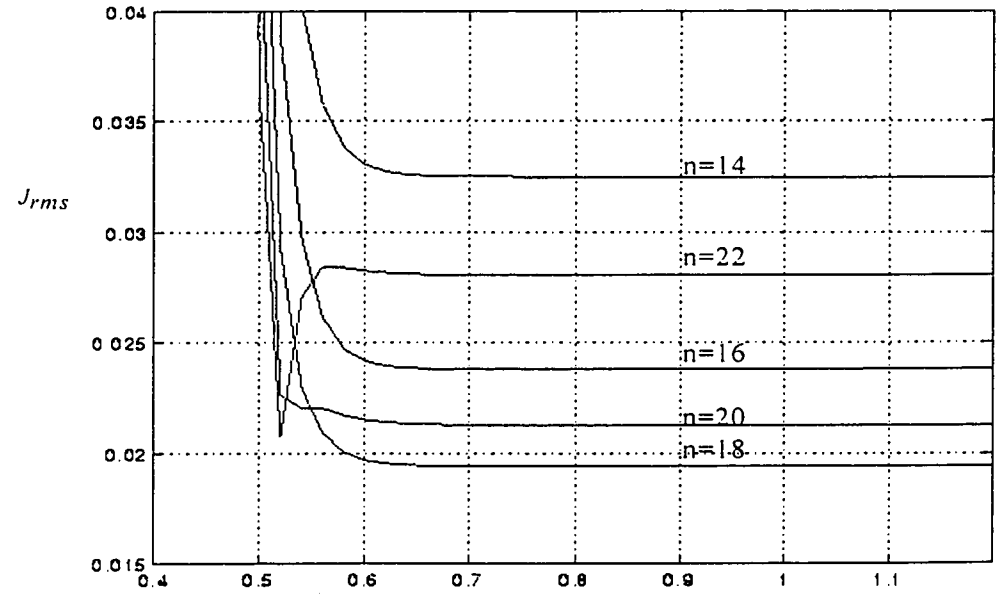

Figure 3.10 - Jitter evaluation with Butterworth filtering, (α=0.1)

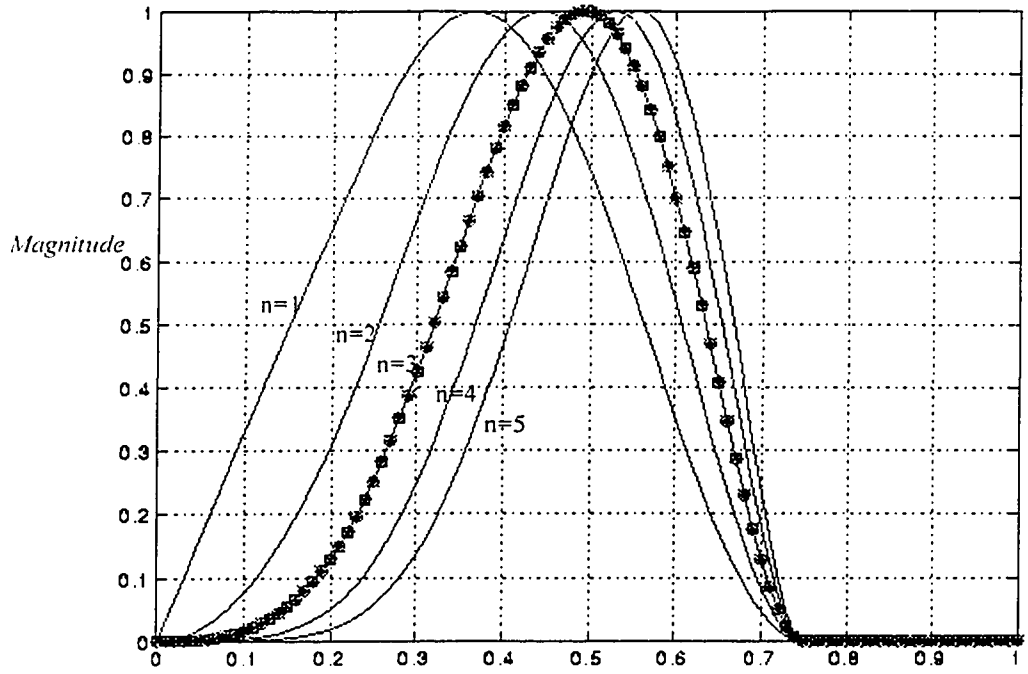

Fig. 3.11 - Spectrum of the prefiltered pulse

Jitter	Ideal Prefilter	No Prefilter	3rd Order Butterworth
2-PAM	0.0037 (rms.)	0.049 (rms.) or ≈ 100 %(p-p)	0.0043 (rms.) or 3.5% (p-p)
4-PAM	0.0038 (rms.)	0.0526 (rms.) or ≈ 100 %(p-p)	0.0047 (rms.) or 4.5% (p-p)
8-PAM	0.0038 (rms.)	0.0561 (rms.) or ≈ 100% (p-p)	0.0048 (rms.) or 5.5 %(p-p)
Note: α=0.5 and the Q of the tuned filter are set to 28.			

Table 3.1- Jitter improvement by the Butterworth prefilter

filter is considered as a single tuned, second order (Series RLC). The results indicate that a proper choice of the Butterworth prefilter, can significantly improve the jitter performance.

3.3.4) Combined Effects of the Butterworth Prefiltering and Q of the Tuned Filter

The fundamental function of the tuned filter, as stated earlier, is to extract the clock frequency component out of the spectrum of the squared signal. Increasing the Q of the tuned filter helps to reduce the jitter. By increasing the Q, the symmetry of the frequency response of the tuned filter - which was stated as the second necessary condition for a jitter-free operation - will be relatively increased. As shown in Figure 3.12, by increasing the Q, jitter performance is improved. However increasing the Q of the tuned filter is not always an appropriate choice. By increasing the Q, system becomes more sensitive to mistuning. Furthermore, the recovery time, which is a very important issue in timing recovery design, will be increased. For a tuned filter (centered at f_o with an order of n and a quality factor of Q) the delay which corresponds to timing recovery time can be approximated as,

$$t_D = \frac{0.25n}{f_o} Q. \tag{3.25}$$

A filter can be made to be more symmetric by increasing the order and/or the Q of the filter. In either case, based on Equation (3.25), it leads to an increase in recovery time.

Referring to Figure 3.12.a and Figure 3.12.b, although the prefilter is not perfectly matched to the spectrum of the transmitted pulse, it is able to ameliorate the operation of

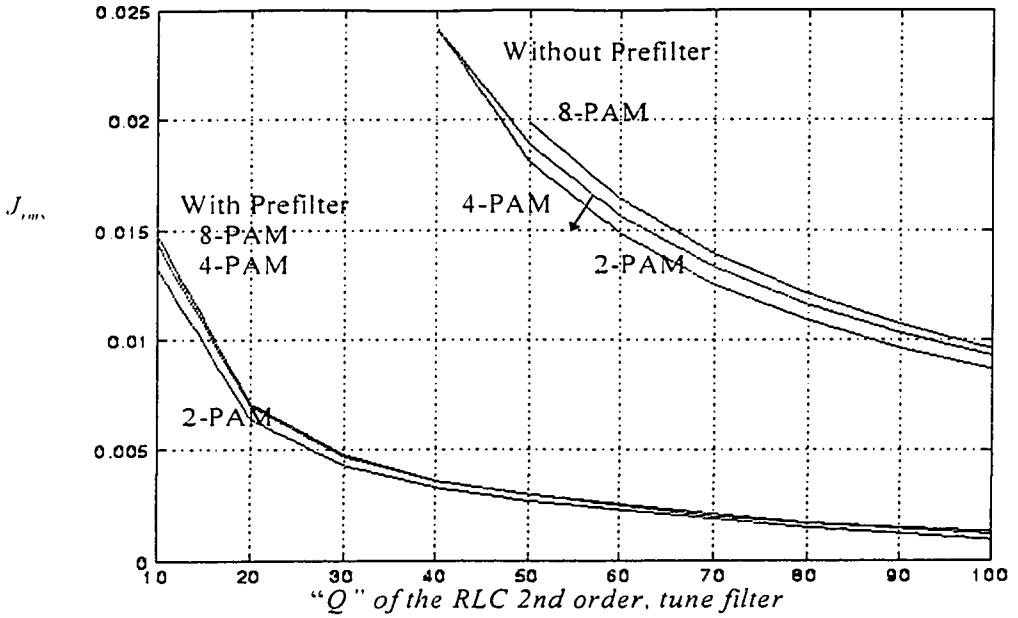

Figure 3.12.a - The jitter (*rms*) variation versus Q for α=0.5

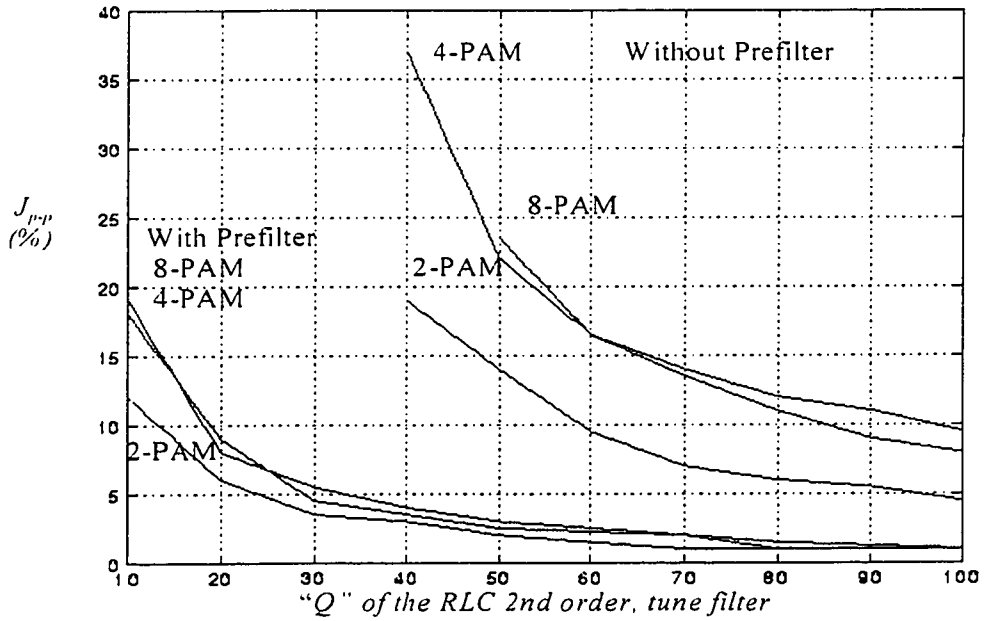

Figure 3.12.b - The jitter (*p-p*) variation versus Q for α=0.5

squarer STR unit. From Figure 3.12.a and Figure 3.12.b, it is observed that by employing the prefilter, the tuned filter can have a lower Q and still operate with the same jitter.

In fact by employing the Butterworth prefilter, high Q requirement of the tuned filter can be relaxed and consequently faster recovery time be expected. For instance, in the case of no prefilter, a tuned filter with $Q=90$ is required to achieve $J_{rms.}=0.01$. However in the case of prefiltering, a wider tuned filter with $Q=16$ can be used to obtain a similar performance. A wider filter implies a faster recovery time.

3.3.5) Effect of the Thermal Noise

Prefiltering helps to improve the noise performance of the STR unit by rejecting low frequency component of the input noise. However, the main parameter controlling the impact of thermal noise on the jitter performance is the bandwidth of the tuned filter. A narrower bandwidth will help to reduce the amount of spurious signals and noise. Jitter performance in presence of thermal noise is examined, using the model shown in Figure 3.5. The receive root-square raised-cosine filter has a roll-off factor of $\alpha=0.5$ (as the transmitter). Base on the results in Sec. 3.3.3, a 3rd order Butterworth filter is selected as the prefilter. The Q of the tuned filter is set to 28. As shown in Figure 3.13.a and Figure 3.13.b, jitter performance degrades by increasing the noise in an exponential form. For all three modulation cases, jitter is high and un-acceptable for practical applications. To improve the jitter performance, Q of the tuned filter has to be selected higher. By increasing the Q, there will be less contribution of both thermal and pattern noise.

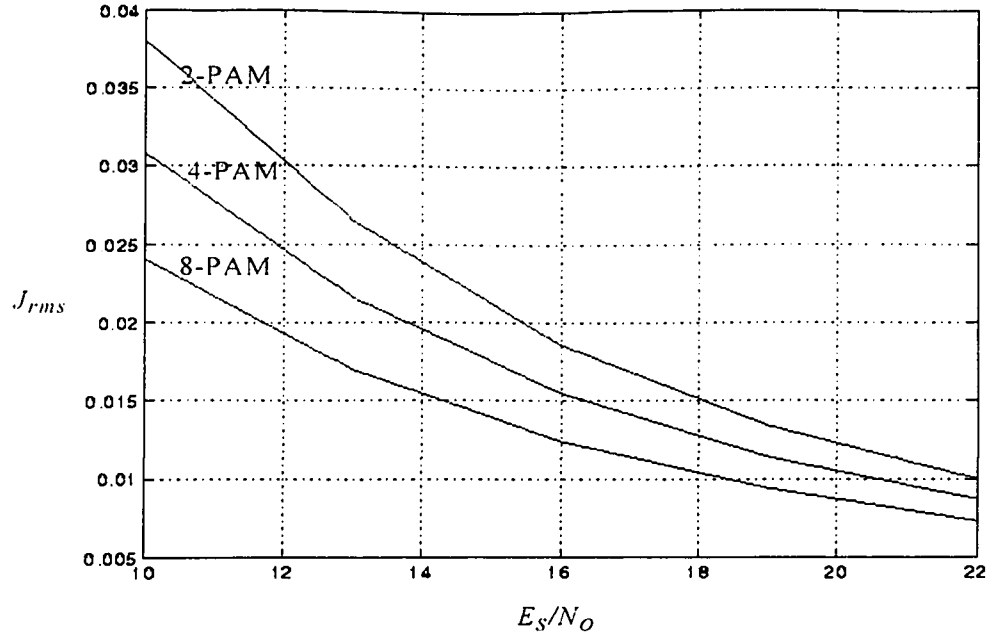

Figure 3.13.a - Noise performance of the squarer STR (J_{rms})

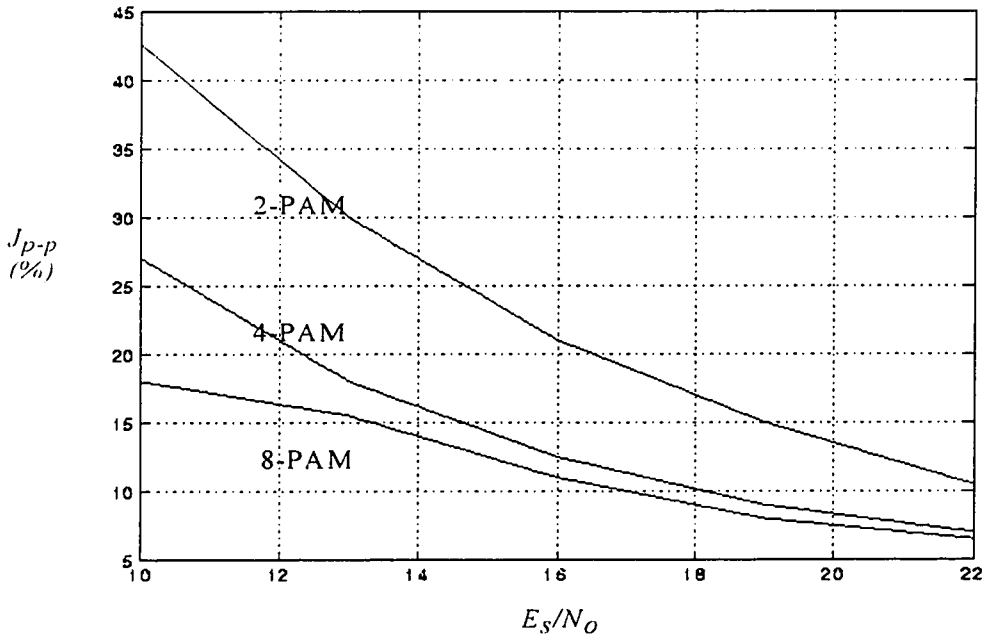

Figure 3.13.b - Noise performance of the unit ($J_{p\text{-}p}$)

3.4) Experimental Results

A squarer STR circuit based on the structure shown in Figure 3.5 was designed and implemented. The detailed schematic of the circuit is shown in Figure 3.15. The experiments were performed to evaluate the effectiveness of prefiltering. A summary of design parameters and the block diagram of the test set-up are presented in Table 3.2 and Figure 3.14, respectively.

Symbol Rate	460Ksymbol/s
Signaling Pulse	Raised-cosine, α=0.5
Prefilter	Butterworth 3rd order, f_C=460KHz
Tuned Filter	RLC single tuned, 2nd order and Q=28
Study Cases	2-PAM, 4-PAM and 8-PAM

Table 3.2 - Squarer circuit design parameters

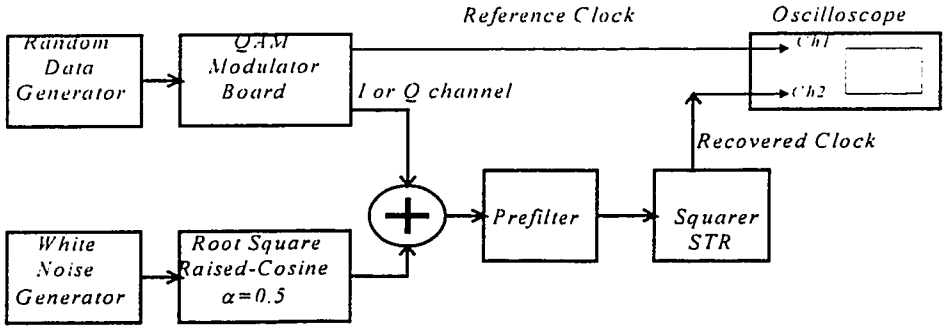

Figure 3.14 - Block diagram of the experimental set-up

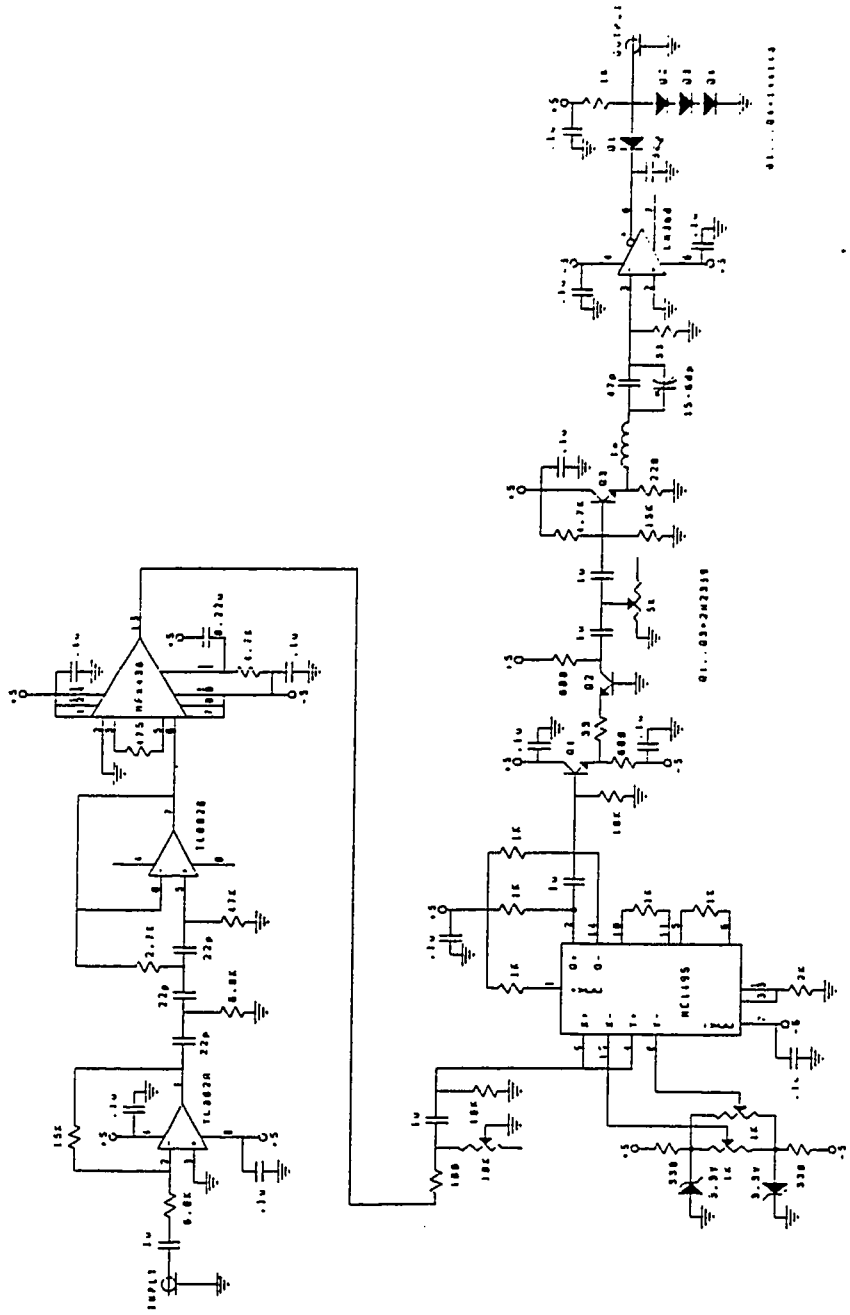

Figure 3.15 - Detailed schematic of the squarer circuit

3.4.1) Squarer with no Prefiltering

In the first step, the prefilter is bypassed and the random pattern is directly delivered to the squarer. In this condition, the recovered signal is extremely jittery and a stable clock signal cannot be obtained for any of the different input signals, Figure 3.16. In Figure 3.17, the spectrum of the input signals and their squared versions for different cases of 2, 4 and 8 level signal are shown. As observed, the spectrum of the squared signal has a discrete tone at the symbol rate frequency. However, the designed circuit was not able to recover the synchronous tone. It can be predicted that by increasing the Q of the tuned filter, the discrete tone can be recovered.

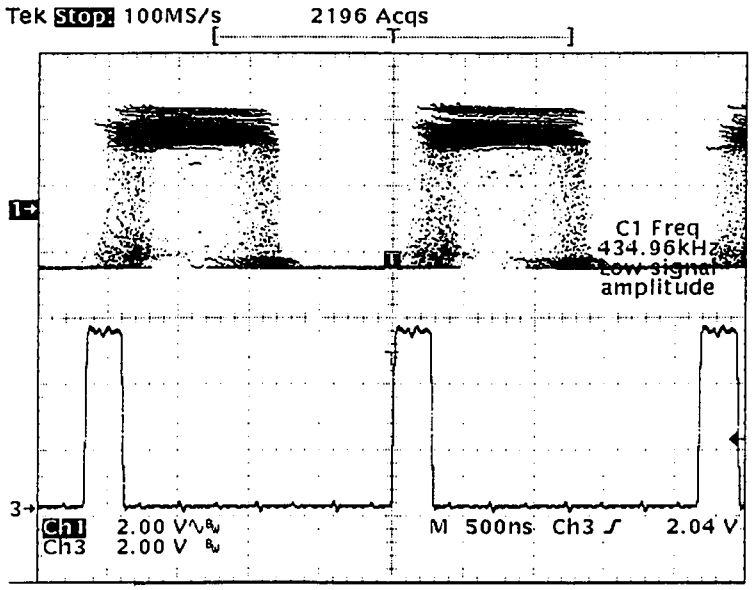

Figure 3.16 - Recovered clock without prefiltering

a) 2-PAM

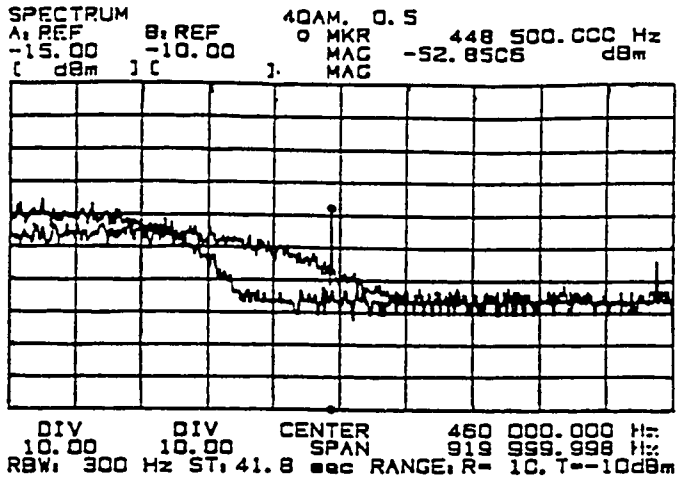

b)4-PAM

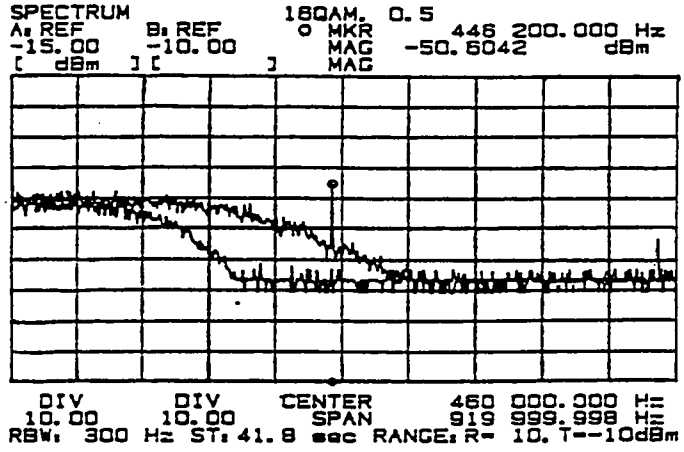

c) 8-PAM

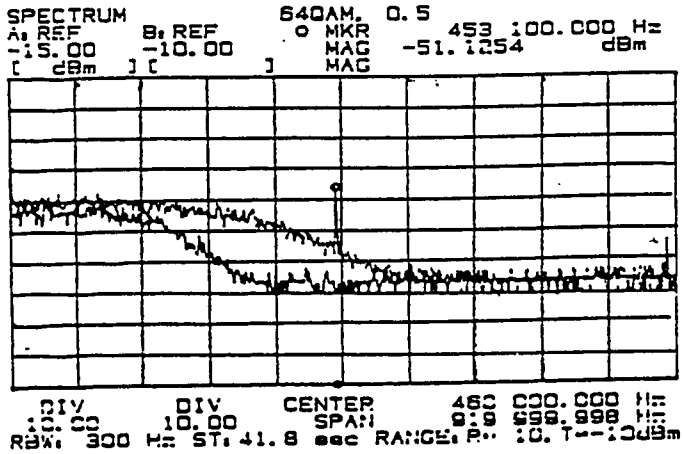

Figure 3.17- Spectrum of the input and output of the squarer without prefiltering for three modulation cases

3.4.2) Squarer with Prefiltering

In the next step, the received signal is first prefiltered and then is fed to the squarer circuit. Figure 3.18 shows the spectra of the input and the prefiltered signals for each case of modulation. As seen, although the 3rd order Butterworth filter is not an ideal replacement for the prefilter, it shapes the input spectrum to a symmetric form about *230KHz* ($1/2T_0$), and bandlimited to *115KHz* and *345KHz* - consistent to the jitter-free requirements. As a result of feeding this fairly symmetric signal to the squarer circuit, the output signal has a symmetric spectrum about the symbol rate with a significant frequency component at the symbol rate, shown in Figure 3.19. In this condition, the clock signal is acquired for all three cases of input signal, Figure 3.20. In each case, the first trace is the transmitter clock which is used as the trigger signal for the oscilloscope. The second trace represents the received signal at the input of the STR unit and the last trace shows the recovered clock. As seen in Figure 3.20, jitter is not zero, however considering the relatively low Q of the employed tuned filter, it is at a reasonable level of about $Jitter_{p\text{-}p}=5\%$. The spectrum of the recovered clock is shown in Figure 3.21. As discussed in the second chapter, the jitter quality of different clock recovery schemes can be judged by measuring the phase noise in frequency domain. Phase noise is measured as the ratio of the power of the clock component to the noise sideband (either side) at a given frequency offset from the clock rate frequency. The ratio by including the resolution bandwidth of the spectrum analyzer is measured as;

$$\text{Phase Noise @10KHz} = 52\text{-}10log(100)=72\text{dBc/Hz}.$$

a) 2-PAM

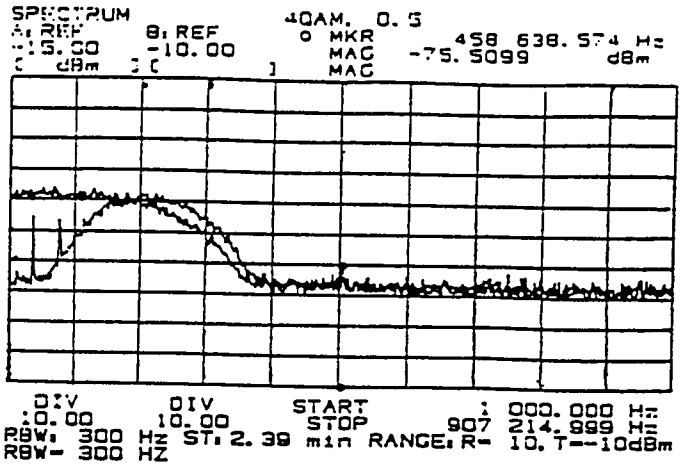

b)4-PAM

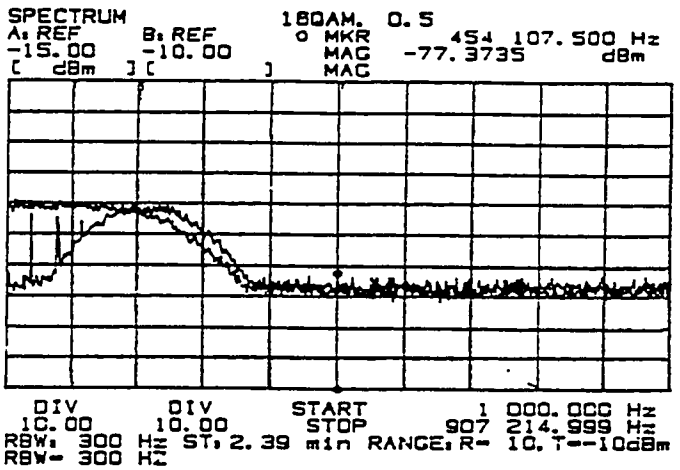

c) 8-PAM

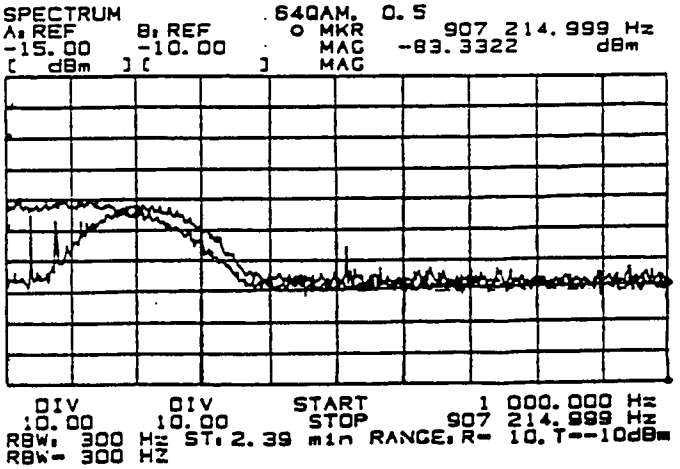

Figure 3.18- Spectrum of the input and output of the prefilter for three modulation cases

a) 2-PAM

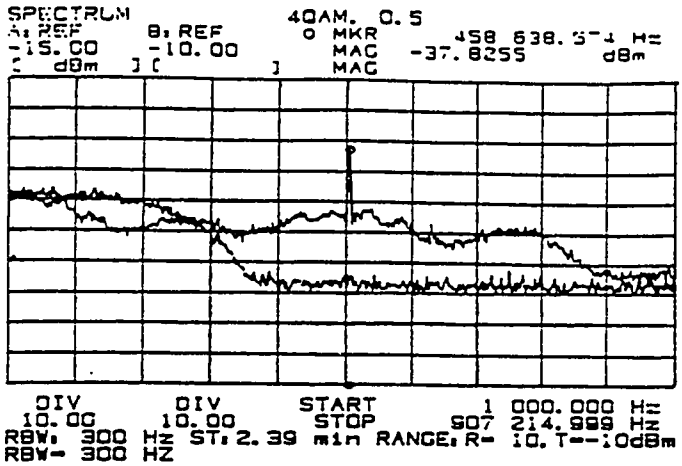

b)4-PAM

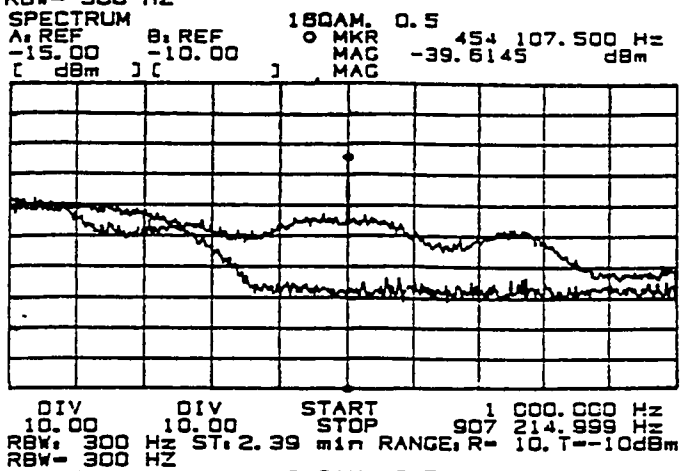

c) 8-PAM

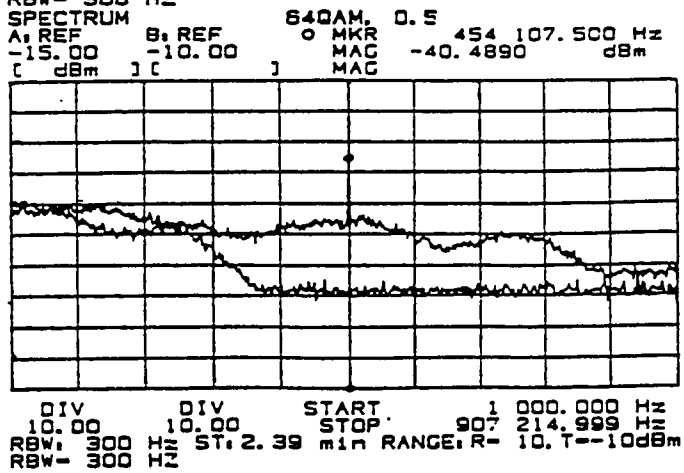

Figure 3.19- Spectrum of the input data and squared of the prefiltered signal for three modulation cases

a) 2-PAM

b)4-PAM

c) 8-PAM

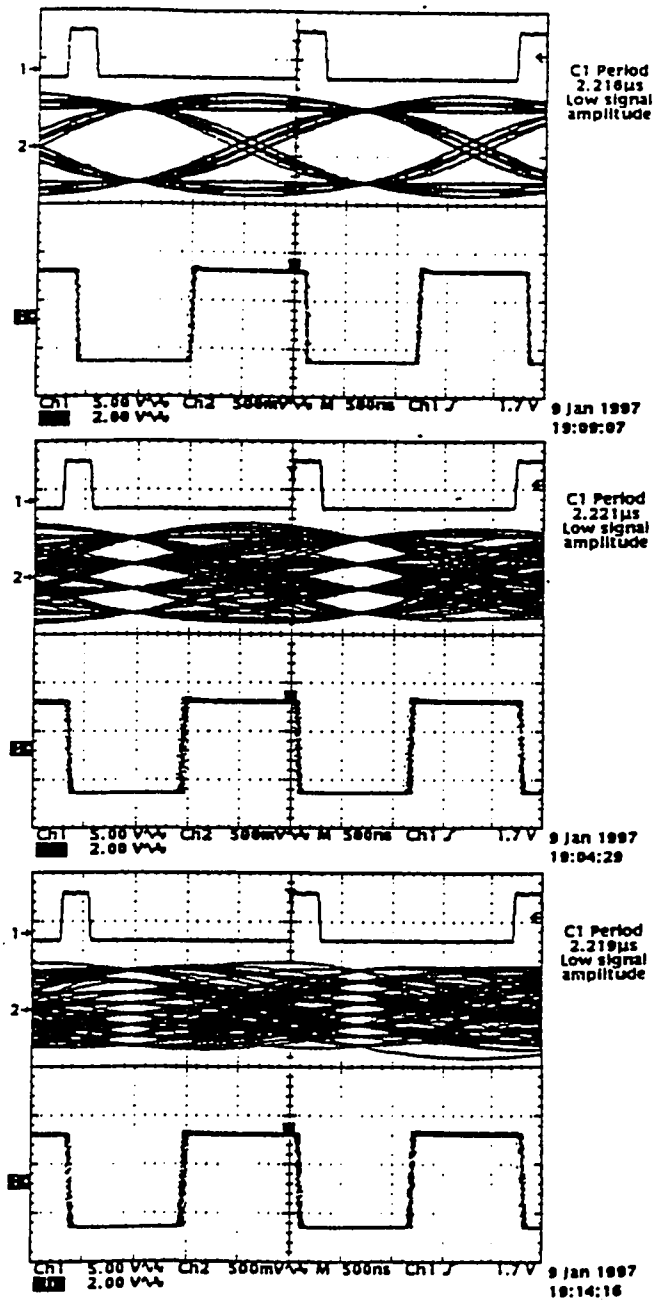

Figure 3.20- Recovered clock by prefiltering, in each graph first trace is the transmitter clock, second is the received data and third is the recovered clock.

a) 2-PAM

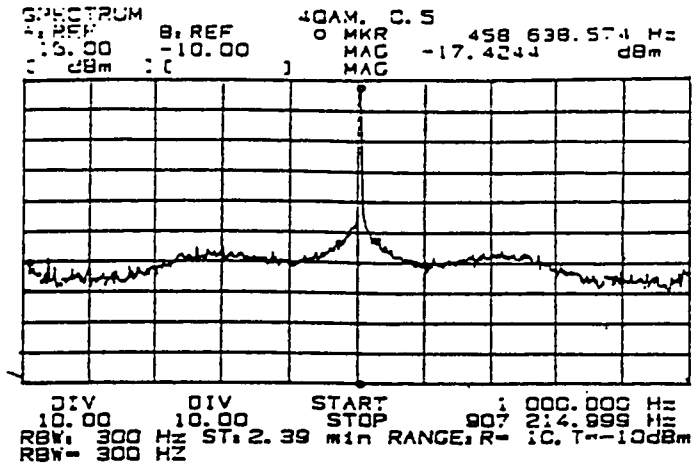

b)4-PAM

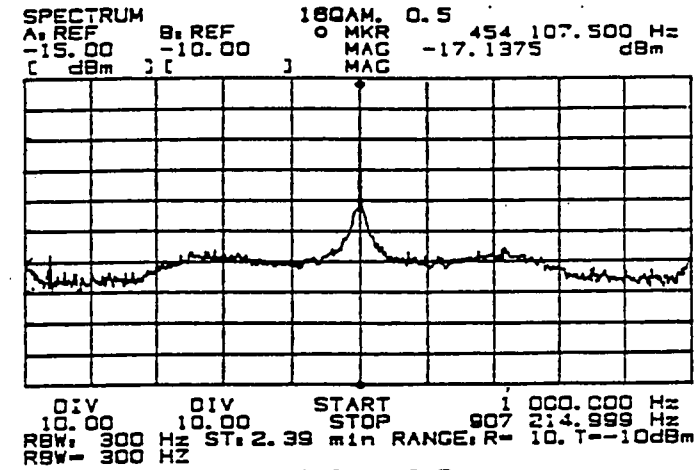

c) 8-PAM

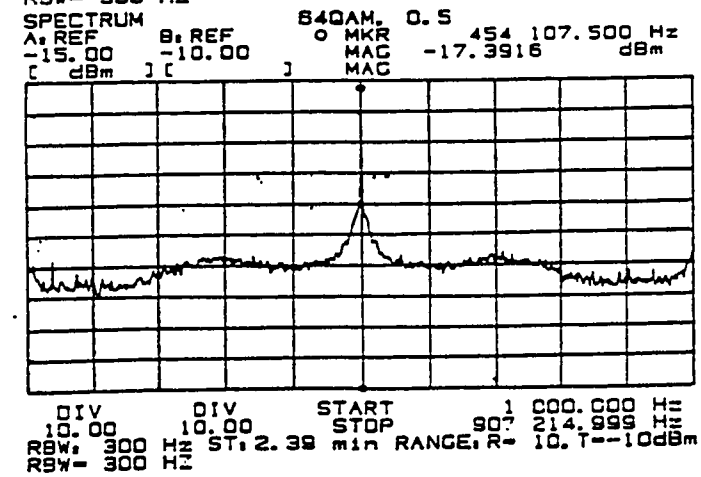

Figure 3.21 - Spectrum of the recovered clock for three modulation cases

3.4.3) Observation: Symmetry of the Spectrum of the Squared Signal

Figure 3.22 and Figure 3.23 show spectra of the squared signal for two cases of prefiltering/no prefiltering. The observation window is 100KHz.. Points A and B indicate the background noise level at ±50KHz offset from the discrete tone (f_A=410KHz, f_B=510KHz). For the both cases, the ratio of discrete tone power to the background noise at a smaller frequency offset of 1KHz from the discrete tone is equal to 46dB. The spectrum of the case with prefiltering (Figure 3.22), maintains this amount for almost the entire band under consideration. However, as illustrated in Figure 3.23, if there is no prefilter, the spectrum of the squared signal exhibits a non-symmetric shape which has an extra noise energy at frequencies lower than the clock component. For this case as shown in Figure 3.23, the power level difference between the two points A and B is almost 13dB, and inside the half power bandwidth of the tuned filter (BW_{3dB}≅17KHz) is about 4dB. The employed tuned filter is a single-tuned resonant tank with a Q=28 and has a slow frequency roll-off of only 6dB/octave. Therefore, the imbalance is effectively transferred to the output, resulting in a bandpass signal with imbalance sidebands. This has a similar effect on the jitter performance as the case that a non-symmetric bandpass filter is used to filter a symmetric bandpass spectrum. As discussed earlier, it does not meet jitter-free requirements and obviously can cause excessive jitter for the timing recovery unit.

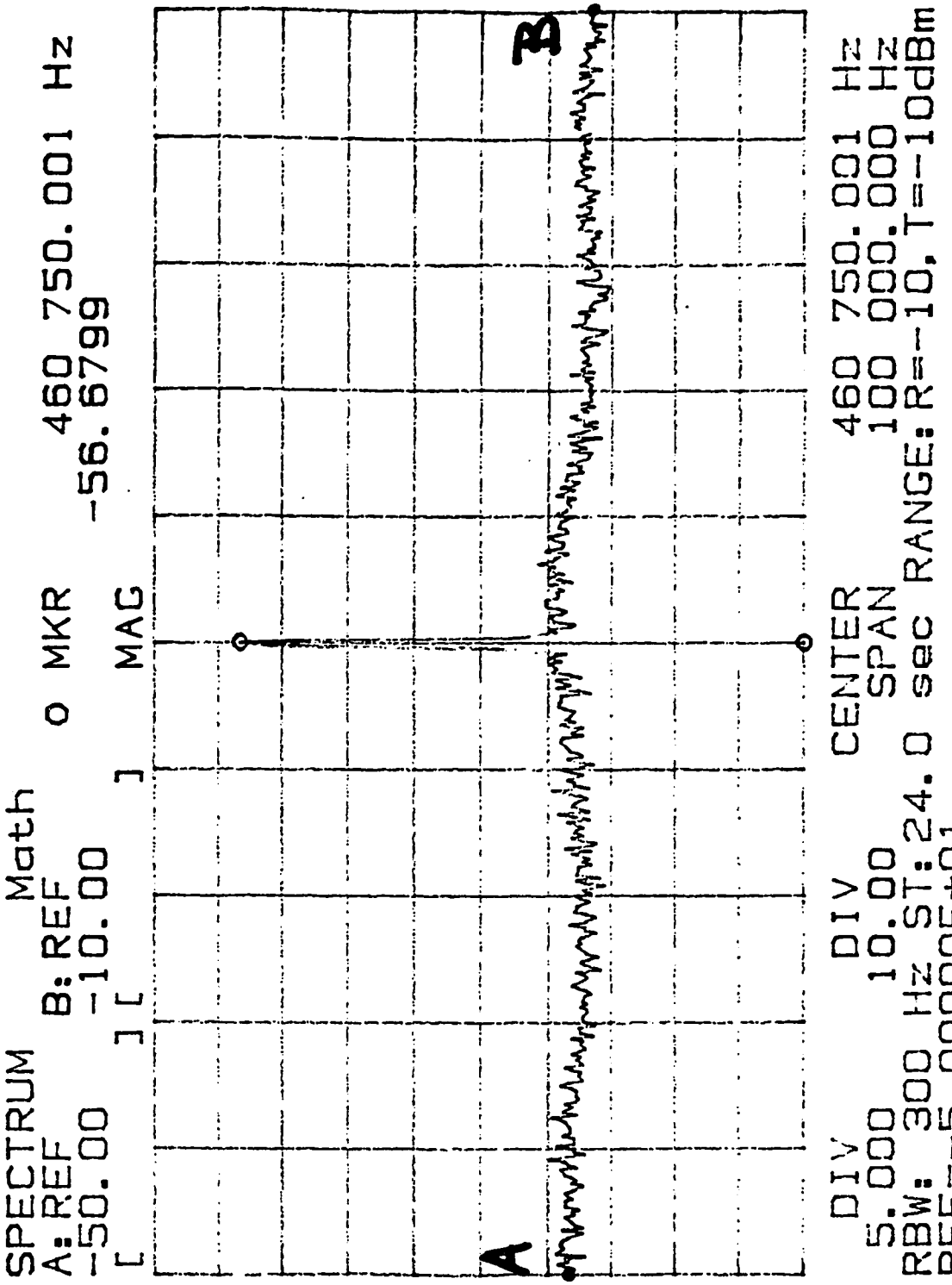

Figure 3.22- Close view of the squared of the prefiltered signal

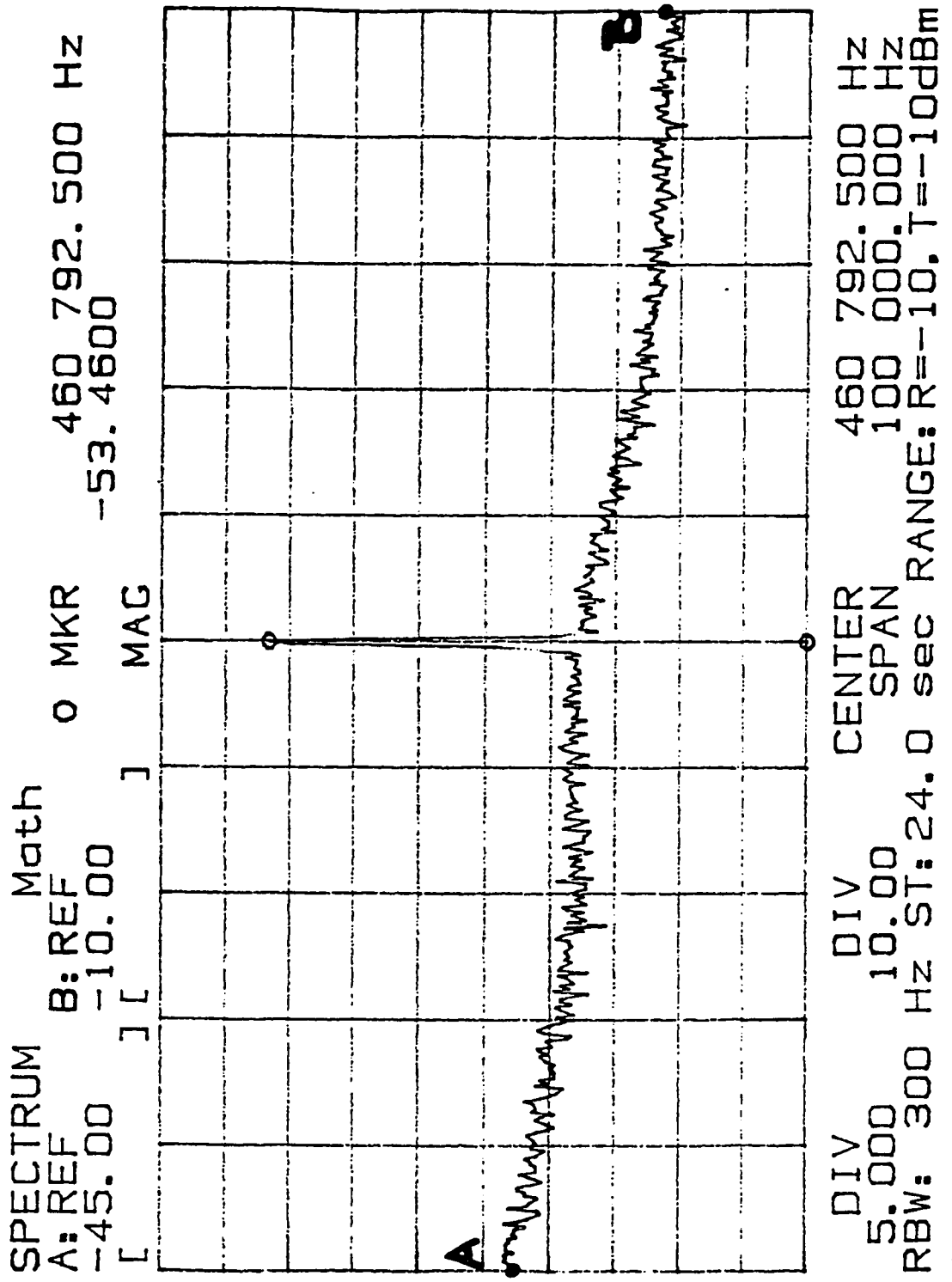

Figure 3.23 - Close view of the squared of the signal without prefiltering

3.4.4) Noise Performance

Figure 3.24 shows the jitter performance of the implemented unit in presence of thermal noise. Comparing to the simulation results in Figure 3.13.b, there are some differences which essentially can be addressed to the employed measurement technique and the implementation impairments. In measuring the jitter by the oscilloscope, the measured jitter is the width of the fluctuated clock edge creating the darkest area on the oscilloscope. In simulations, all clock transitions are considered for peak to peak jitter measurement of the recovered clock, however in measurement by using oscilloscope, fluctuations with large swings (due to the less likelihood of their occurrence) are ignored. As shown in Figure 3.24, a 10dB decrease in E_S/N_O results in 50% increase in the peak to peak jitter. This may not be acceptable for most applications. To reduce the effect of thermal noise on the jitter performance, Q of the tuned filter has to be increased.

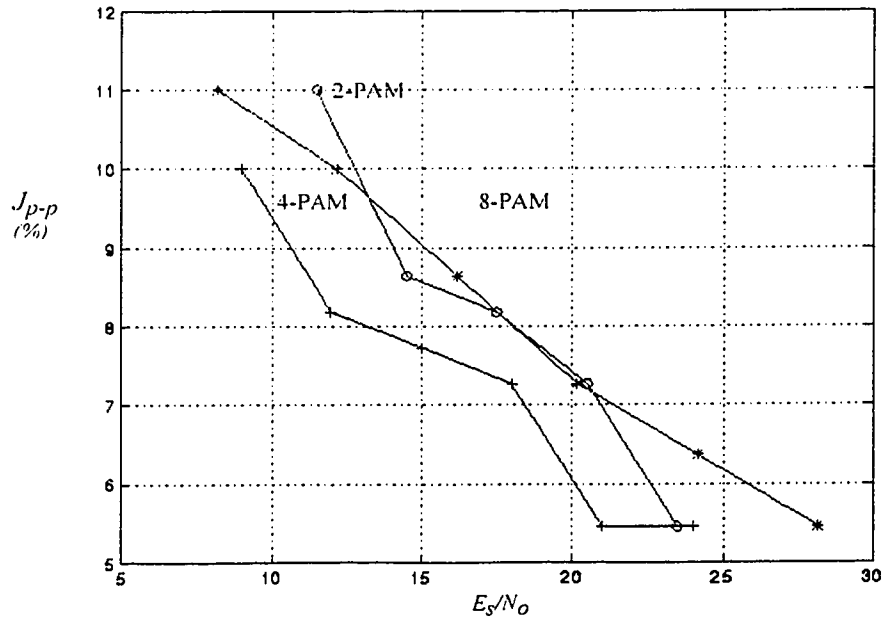

Fig. 3.24 - Noise performance test of the implemented unit

3.5) Discussion and Summary

This chapter dealt in analyzing jitter performance of the squarer timing recovery with prefiltering for M-ary signals. Several simulations were done to study the effect of imperfections of the prefilter and the bandpass filter. A prototype of the scheme was implemented and tested. Based on the simulation and experiment results, the following can be summarized:

- Although an ideal prefilter which matches to the spectrum of the input signal cannot be realized, an optimum Butterworth prefilter can improve jitter performance of the squarer scheme. The effectiveness of prefiltering is more appreciated when a narrow-band bandpass filter cannot be employed.
- Besides the Q of the clock filter, the symmetry requirement of the tuned filter is another important issue that must be taken into the account. In other words, providing the symmetry of the tuned filter, the Q of the tuned filter can be considered as a second hand priority for the bandpass filter design.
- The performance of the squarer with prefiltering is less influenced by the level of modulation (M-PAM).

Chapter 4

COSTAS LOOP TIMING SYNCHRONIZER

In the squarer timing recovery, prefiltering is required to achieve zero jitter. In practice, it is quite difficult to design a prefilter properly matched to the received signal, hence the performance is poor. A low jitter symbol timing recovery based on the Costas loop is presented. The equivalence between the introduced Costas and the zero-jitter squarer is discussed. The Costas STR scheme eliminates the need of prefiltering, moreover it avoids the use of the nonlinear function. The Costas STR scheme can practically achieve an extremely low jitter performance.

4.1) Costas Loop Timing Recovery Concept

To achieve zero jitter in the squarer STR (Figure 3.1), the input signal $x(t)$, to the squarer has its spectrum symmetric about $1/2T_o$. Hence, it can be considered as a double side-band suppressed carrier (DSB-SC) signal, centered at $1/2T_o$ and having a bandwidth

of $1/2T_o$. In other words, it can be written as $x(t)=\Omega(t)\cos(\pi t/T_o)$, where $\Omega(t)$ is a baseband signal band-limited to $1/2T_o$. Based on this view, the subsequent blocks, i.e., the squarer and the bandpass filter $V(f)$ essentially play the role of a carrier recovery sub-system to regenerate the second harmonic of the suppressed carrier at $1/2T_o$. Squarer generates the desired carrier component and the tuned filter extracts it. Alternatively, a Costas loop can be used to recover the suppressed carrier of such a DSB-SC [9],[12],[13]. Figure 4.1 shows a Costas loop to replace the squarer and bandpass filter in Figure 3.1. It consists of two mixers M_1 and M_2, two identical lowpass filters $M(f)$ at each arm, a multiplier M_3 and the loop filter $L(f)$ - to produce the error signal - and finally a voltage controlled oscillator (VCO) to generate the desired locked signal. The mixers M_1 and M_2 are derived by two in-phase and quadrature versions of the VCO signal, respectively. In Figure 4.2, frequency domain presentations of signals at different points of the system are illustrated. The input signal $r(t)$ to the prefilter has a raised-cosine spectrum shown by trace a. Trace b represents the frequency response of the prefilter matched to the spectrum of $r(t)$ in order to produce an output signal $x(t)$ that has a symmetric, bandlimited spectrum as previously defined by Eq.(3.23) and shown by trace c in Figure 4.2. Signal $x(t)$ is multiplied by $\cos(2\pi t/2T_o)$ and $\sin(2\pi t/2T_o)$. The spectrum of the output signals of the mixers M_1 and M_2 are shown by traces d and e. The lowpass filters $M(f)$ have an identical frequency response. The bandwidth is selected to be wider than the single-sided bandwidth of $x(t)$ in order to reject the high-frequency components centered at $\pm 1/T_o$ and to maintain the baseband component. The filtered versions of the signals are shown in traces f and g (Figure 4.2). As seen, the prefiltering has basically no decisive

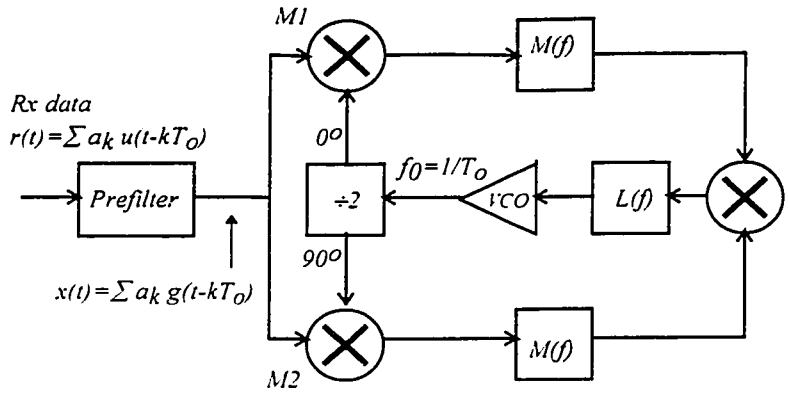

Figure 4.1- Costas loop with pre-filtering

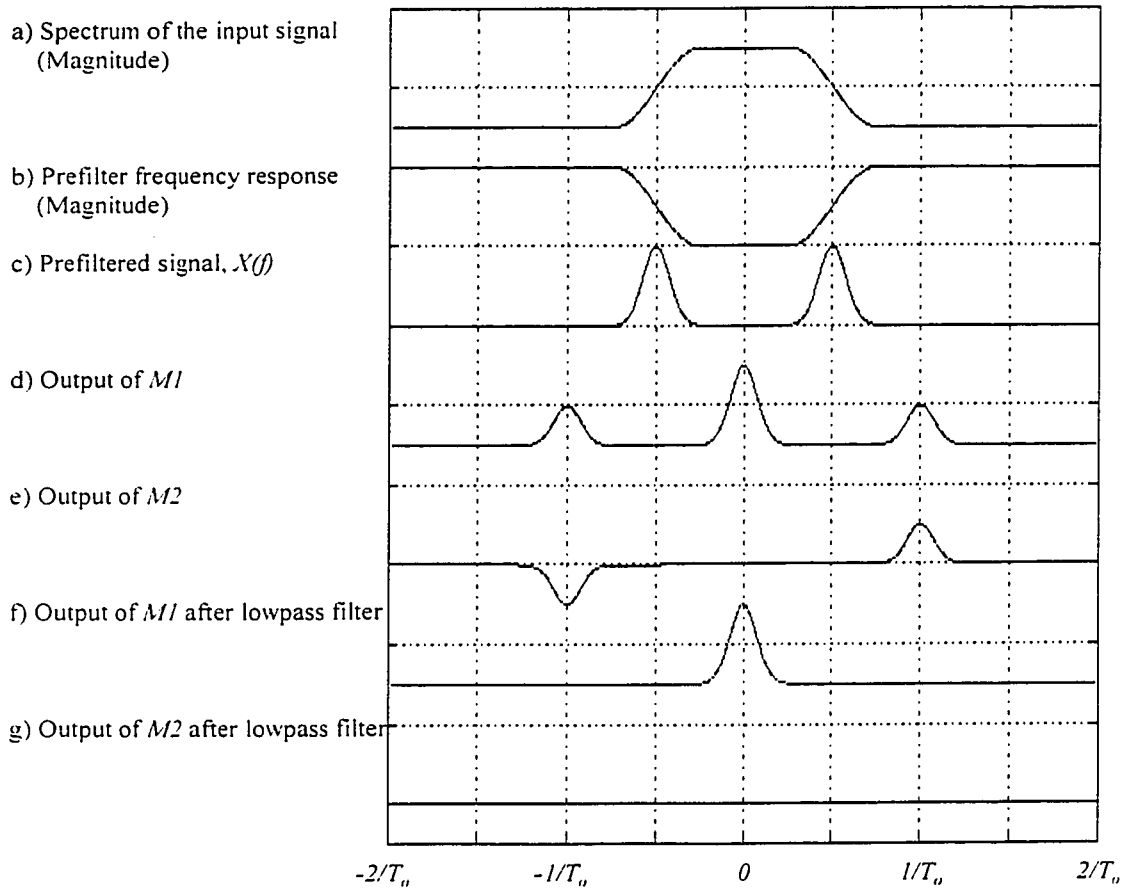

Figure 4.2 - Frequency domain representation of signals of the system shown in Figure 4.1

effect inside the loop and due to the frequency translation, it has changed to a lowpass signal. As will be explained, this fact is useful in simplifying the proposed scheme.

Figure 4.3 shows an equivalent circuit in which the prefilter is removed. The input to the Costas loop is *r(t)* with the spectrum shown in Figure 4.4, trace a. Accordingly, the output of the mixer at the upper arm has a spectrum shown by trace b in Figure 4.4. Note that, due to the symmetry of the raised-cosine shape about the Nyquist frequency, overlapping the two sides of its spectrum creates a flat spectrum about the zero frequency as shown by trace b. At the other branch, the two sides of the spectrum, as the result of the frequency translation, subtract from each other and create a spectrum with an odd symmetry about the zero frequency. At the upper branch, in order to provide a similar spectrum of the baseband component shown in Figure 4.2 (trace f), the lowpass filter *H(f)* should have a frequency response shown by trace d of Figure 4.4. In other words, the pre-filter and lowpass filter *M(f)* in Figure 4.1 can be replaced by one lowpass filter *H(f)*. Furthermore, *H(f)* is actually the lowpass equivalence of *G(f)*. However, since *H(f)* is a lowpass filter, the symmetry requirement is already met, and there is no need to match to the spectrum of *u(t)*. The trace f of Figure 4.4 shows the spectrum of the signal at the lower arm. Although the spectrum is not similar to the trace g of Figure 4.2, it has an odd symmetry characteristic. As will be shown in the next section, it helps to have a phase detection process similar to the Costas loop scheme used for carrier recovery.

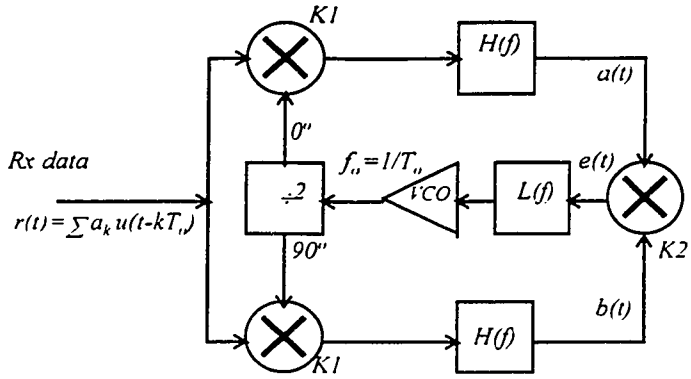

Figure 4.3 STR Costas architecture

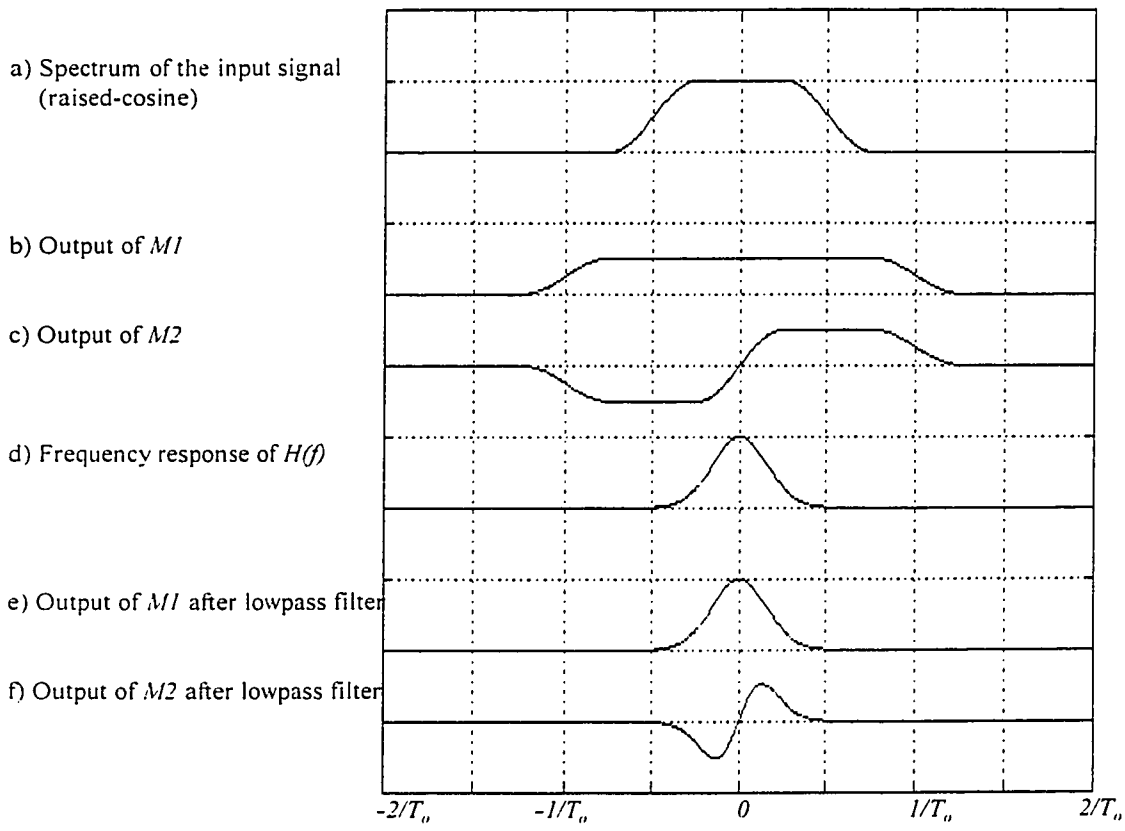

Fig. 4.4 - Frequency domain representation of signals of the Costas STR

A comparison between these two cases (Figure 4.2 and Figure 4.4) shows that by employing a lowpass filter *H(f)* after the mixer at each branch, we can avoid the prefilter and technically obtain the same result.

4.2) Phase Detection Process

In Figure 4.3, *u(t)* has a raised-cosine spectrum. Mixers are characterized by conversion gain K_1 and K_2. The lowpass filters *H(f)* are assumed having a rectangular frequency response with a bandwidth of $B<<1/T_O$.

For a given phase error θ_e, the output signals of the lowpass filters at each arm can be written as:

$$a(t) = K1\sum_k a_k u(t - kT_o)Cos(\frac{\omega_o t}{2} + \theta_e) * h(t) \tag{4.1.a}$$

$$b(t) = K1\sum_k a_k u(t - kT_o)Sin(\frac{\omega_o t}{2} + \theta_e) * h(t). \tag{4.1.b}$$

Expanding the sine and cosine terms,

$$a(t) = K_1 Cos\theta_e \sum_k a_k c(t - kT_o) - K_1 Sin\theta_e \sum_k a_k s(t - kT_o) \tag{4.2.a}$$

$$b(t) = K_1 Cos\theta_e \sum_k a_k s(t - kT_o) + K_1 Sin\theta_e \sum_k a_k c(t - kT_o), \tag{4.2.b}$$

where,

$$c(t) = u(t)Cos(\frac{\omega_o t}{2}) * h(t) \tag{4.3.a}$$

$$s(t) = u(t)Sin(\frac{\omega_o t}{2}) * h(t). \tag{4.3.b}$$

The Fourier transforms of *c(t)* and *s(t)* are shown in Figure 4.5. The error signal at the input of the loop filter is given by:

$$e(t) = a(t)b(t). \tag{4.4.a}$$

$$\begin{aligned} e(t) = {} & K_1^2 K_2 Cos^2\theta_e \sum_k a_k c(t-kT_o) \sum_k a_k s(t-kT_o) \\ & + K_1^2 K_2 Cos\theta_e Sin\theta_e \left(\sum_k a_k c(t-kT_o) \right)^2 \\ & - K_1^2 K_2 Cos\theta_e Sin\theta_e \left(\sum_k a_k s(t-kT_o) \right)^2 \\ & - K_1^2 K_2 Sin^2\theta_e \sum_k a_k c(t-kT_o) \sum_k a_k s(t-kT_o). \end{aligned} \tag{4.4.b}$$

It can be rewritten as:

$$\begin{aligned} e(t) = {} & K_1^2 K_2 Cos2\theta_e \sum_k a_k c(t-kT_o) \sum_k a_k s(t-kT_o) \\ & + \frac{K_1^2 K_2}{2} Sin2\theta_e \left\{ \left(\sum_k a_k c(t-kT_o) \right)^2 - \left(\sum_k a_k s(t-kT_o) \right)^2 \right\}. \end{aligned} \tag{4.5}$$

The loop filter $L(f)$ produces the average of $e(t)$,

$$\overline{e(t)} = K_1^2 K_2 Cos2\theta_e . \lambda_1 + \frac{K_1^2 K_2}{2} Sin2\theta_e . \lambda_2 \tag{4.6}$$

where,

$$\begin{aligned} \lambda_1 &= E\left[\sum_k a_k c(t-kT_o) \sum_k a_k s(t-kT_o) \right] \\ &= E\left[\sum_k \sum_m a_k a_{k+m} c(t-kT_o) s(t-kT_o-mT_o) \right] \\ &= \sum_k \sum_m E\left[a_k a_{k+m} \right] c(t-kT_o) s(t-kT_o-mT_o), \end{aligned} \tag{4.7.a}$$

$$\lambda_2 = E\left[\left(\sum_k a_k c(t-kT_o) \right)^2 \right] - E\left[\left(\sum_k a_k s(t-kT_o) \right)^2 \right]. \tag{4.7.b}$$

Since $\{a_k\}$ is a statistically independent random sequence (Section 2.1), then:

$$\begin{aligned} & E[a_k a_l] = 0, \quad \text{for} \quad k \neq l \\ & \lambda_1 = E[a^2] \sum_k c(t-kT_o) s(t-kT_o). \end{aligned} \tag{4.8}$$

By applying Poisson formula, Eq.(4.8) can be rewritten as:

$$\lambda_1 = \frac{E[a^2]}{T_o}\sum_l C_f(f)*S_f(f)\Big|_{f=\frac{l}{T_o}} \exp(\frac{j2\pi l}{T_o}), \tag{4.9}$$

where $C_f(f)$ and $S_f(f)$ are Fourier transforms of $c(t)$ and $s(t)$, respectively (Figure 4.5). Exercising the same procedure for Eq.(4.9.b) yields:

$$\lambda_2 = \frac{E[a_k^2]}{T_o}\left\{\sum_l C_f(f)*C_f(f)\Big|_{f=\frac{l}{T_o}} \exp(\frac{j2\pi l}{T_o}) - \sum_l S_f(f)*S_f(f)\Big|_{f=\frac{l}{T_o}} \exp(\frac{j2\pi l}{T_o})\right\}. \tag{4.10}$$

Since the bandwidth B of $H(f)$ is much less than $1/T_o$, convolution terms in Eq.(4.9) and Eq.(4.10) are bandlimited to maximum frequency of $2B$. Hence, they have to be evaluated only for $l=0$,

$$\lambda_1 = \frac{E[a_k^2]}{T_o} C_f(f)*S_f(f)\Big|_{f=0} \tag{4.11.a}$$

$$\lambda_2 = \frac{E[a_k^2]}{T_o}\left\{ C_f(f)*C_f(f)\Big|_{f=0} - S_f(f)*S_f(f)\Big|_{f=0}\right\}. \tag{4.11.b}$$

For the first convolution term we have,

$$C_f(f)*S_f(f)\Big|_{f=0} = \int_{-B}^{+B} C_f(f)S_f(f)df. \tag{4.12.a}$$

$C_f(f)S_f(f)$ is an odd symmetric function, therefore

$$C_f(f)*S_f(f)\Big|_{f=0} = 0. \tag{4.12.b}$$

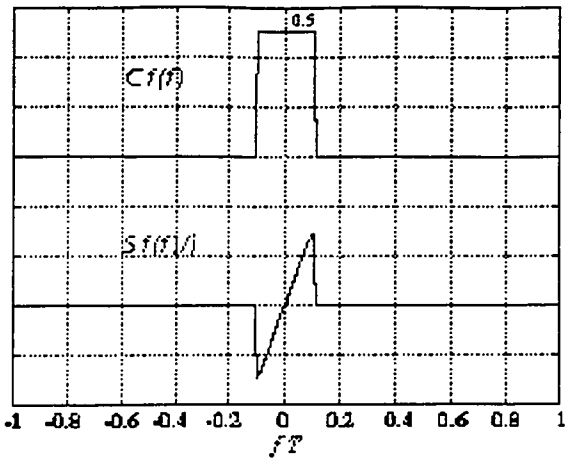

Figure 4.5- Fourier transforms of *c(t)* and *s(t)*

By referring to Figure 4.5:

$$C_f(f)*C_f(f)\Big|_{f=0} = \int_{-B}^{+B} C_f(f)^2 df = \int_{-B}^{+B} (0.5)^2 df = \frac{B}{2}. \tag{4.13}$$

We can approximate $S_f(f)$ to a first order polynomial of f,

$$S_f(f) \approx jmf,$$

$$m = \left| d\frac{U(f)}{df} \right|_{f=\frac{1}{2T_o}} = \frac{\pi T_o}{2\alpha}$$

$$S_f(f) = j\left(\frac{\pi T_o}{2\alpha}\right) f \tag{4.14}$$

where $U(f)$ and α are the spectrum and the roll-off factor of the raised-cosine signal.

$$S_f(f)*S_f(f)\Big|_{f=0} = \int_{-B}^{+B} \left(\frac{j\pi T_o f}{2\alpha}\right)\left(-\frac{j\pi T_o f}{2\alpha}\right) df = \frac{\pi^2 T_o^2 B^3}{6\alpha^2}. \tag{4.15}$$

Results can be finalized as:

$$\lambda_1 = 0, \tag{4.16.a}$$

$$\lambda_2 = \frac{E[a^2]}{T_o}\left\{\frac{B}{2} - \frac{\pi^2 T_o^2 B^3}{6\alpha^2}\right\}, \tag{4.16.b}$$

$$\overline{e(t)} = \frac{BK_1^2 K_2}{4T_u} E[a^2] Sin2\theta_e \left\{ 1 - \frac{\pi^2 T_u^2 B^2}{3\alpha^2} \right\}. \quad (4.17)$$

If we assume further, the bandwidth B of $H(f)$ is much smaller than α/T_o, the transition bandwidth of the raised-cosine spectrum, the error signal can be expressed as:

$$\overline{e(t)} = \frac{BK_1^2 K_2}{4T_u} E[a_k^2] Sin2\theta_e \quad \text{if } B << \frac{\alpha}{T_u}. \quad (4.18)$$

4.3) Experimental Results

An experimental circuit based on the block diagram shown in Figure 4.3 was designed and implemented. The detailed circuit schematic is shown in Figure 4.6. The received pulse $u(t)$ has a raised-cosine spectrum with $\alpha=0.5$. The circuit was tested for three cases of 2-, 4- and 8-PAM. In each case, the symbol rate was fixed at *460KHz*, to maintain the same bandwidth for $H(f)$. The filters ($H(f)$), are single-pole RC lowpass filters with a small bandwidth of *20KHz* (much smaller than α/T_o=*230KHz*). A summary of the design parameters is given in Table 4.1.

Symbol rate	460Ksymbol/s
Signaling pulse	Raised-cosine, α=0.5
Prefilter	Not employed
Arm filter	RC single pole, f_C=20KHz
Loop filter	Lead-Lag filter, f_p=3.5Hz, f_z=1KHz
Study cases	2-PAM, 4-PAM and 8-PAM

Table 4.1 - Design parameters for Costas STR

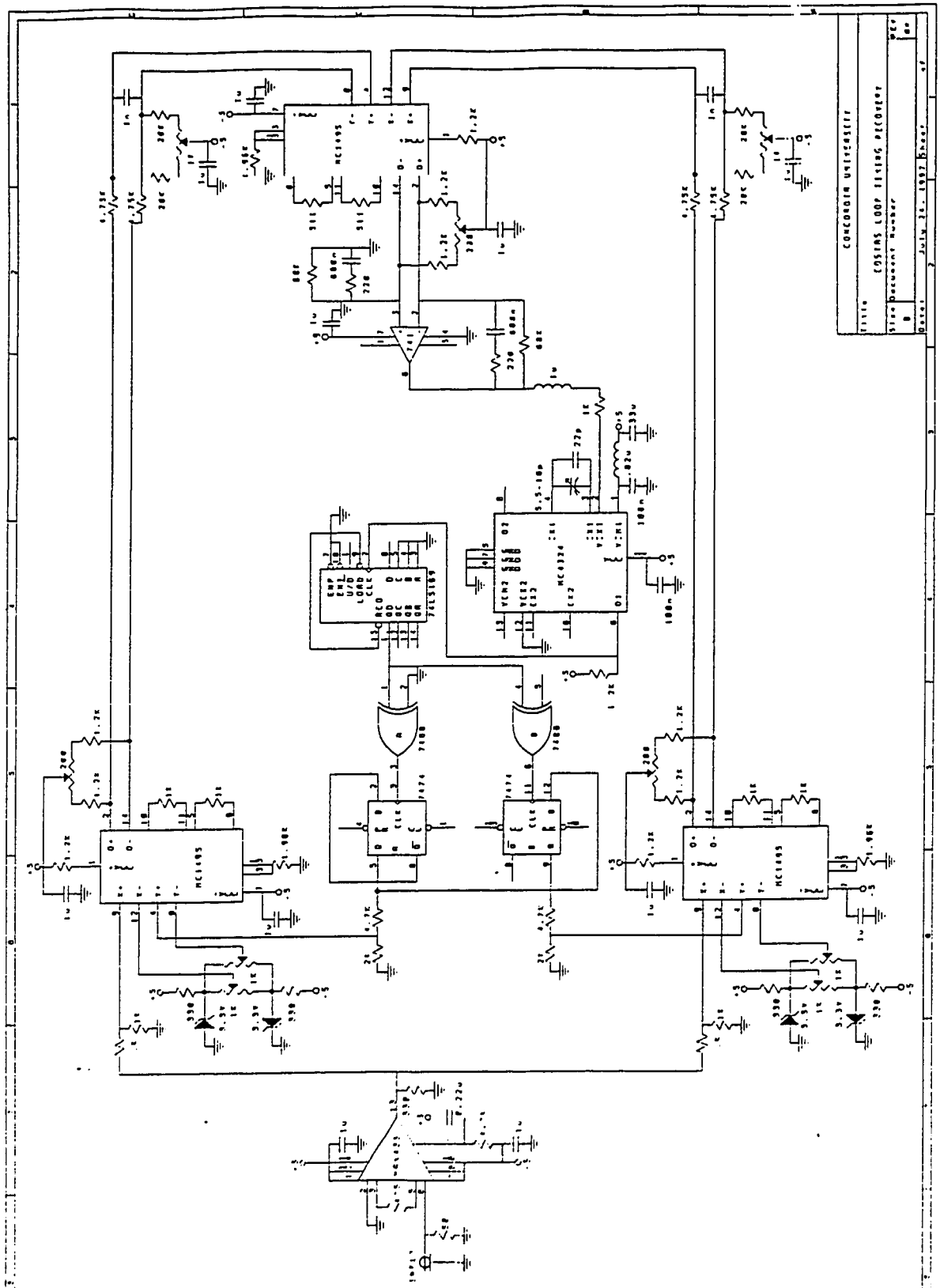

Figure 4.6 - Detailed schematic of the Costas-loop STR

4.3.1) Jitter Performance

Jitter performances of the implemented unit for three cases of 2-, 4- and 8-PAM signals are shown in Figure 4.7. In each case, the first trace shows the transmitter clock. This clock is used as the reference signal for jitter measurement. The second trace is the received signal at the input of the STR. And finally, the third trace represents the recovered clock. The measured peak to peak value for the jitter ($J_{p\text{-}p}$) is about two percent.

Spectra of the recovered clocks for each case of the input signal are illustrated in Figure 4.8, showing the purity of the clock component. As discussed before, phase noise measurement in the frequency domain can be used for jitter performance evaluation of different approaches. The measurement done in the previous chapter, for the squarer timing recovery, indicated a phase noise of 72dBc at 10KHz offset. Now, based on the Figure 4.8, the similar measurement gives,

$$\text{Phase noise @10KHz} = 64\text{-}10log(100)=84\text{dBc/Hz},$$

which shows a 12dB phase noise improvement without any need to prefiltering.

4.3.2) Noise Performance

The same experimental set-up as previously shown in Figure 3.5 is used to examine the noise performance of the implemented unit. Figure 4.9 shows the peak to peak jitter versus E_S/N_O. Comparing to the implemented unit in the preceding chapter, for $E_S/N_O=10dB$, jitter of the Costas STR is almost four times lower than the squarer STR.

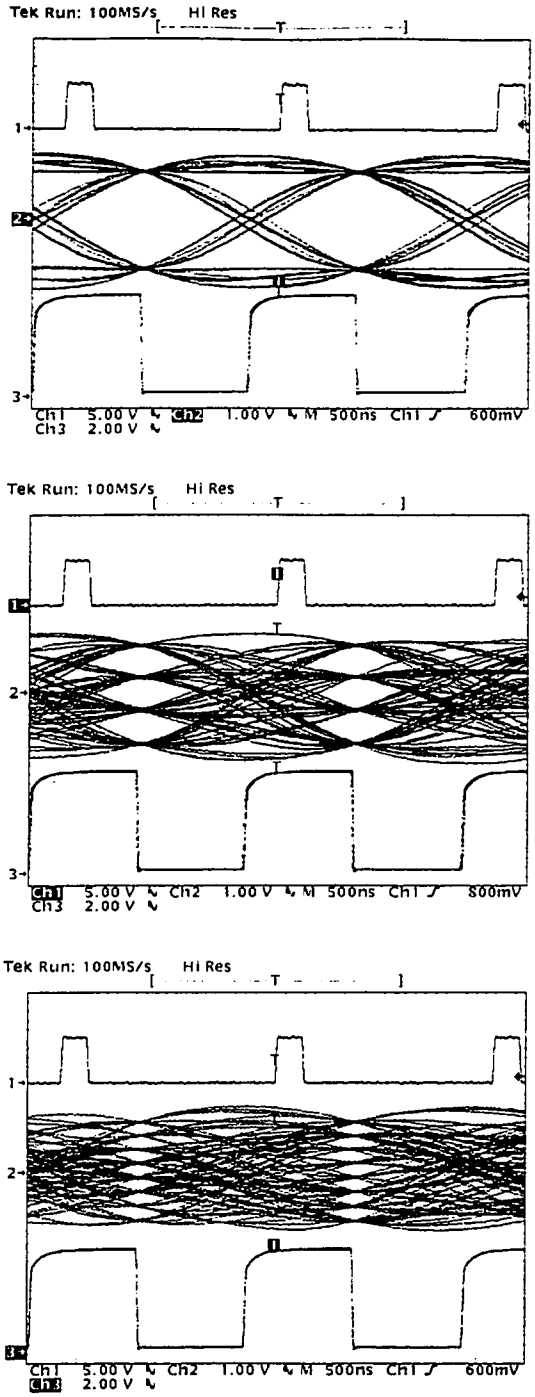

Figure 4.7-Test results for three cases of 2-, 4-, and 8-PAM. In each graph, the first trace represents the transmitter clock, the second is the received data and the third trace shows the recovered clock.

a)2-PAM

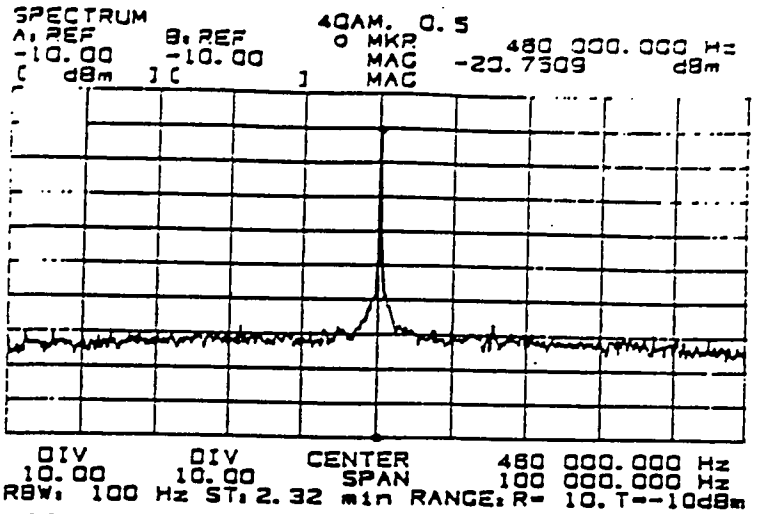

b)4-PAM

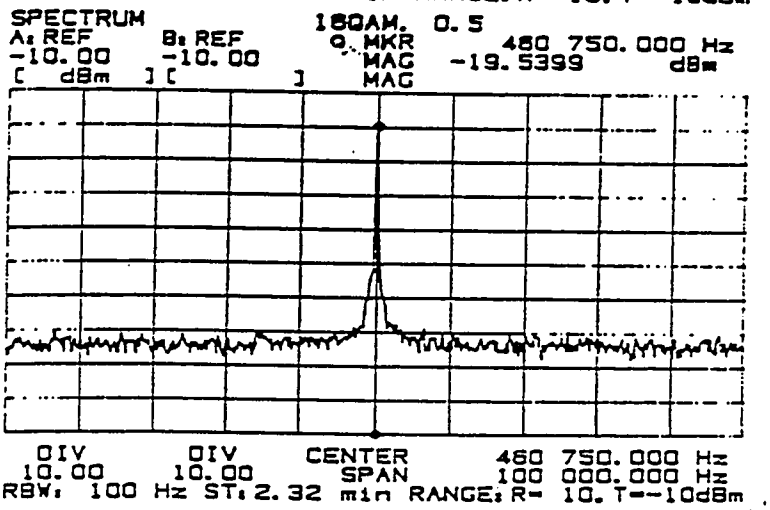

c)8-PAM

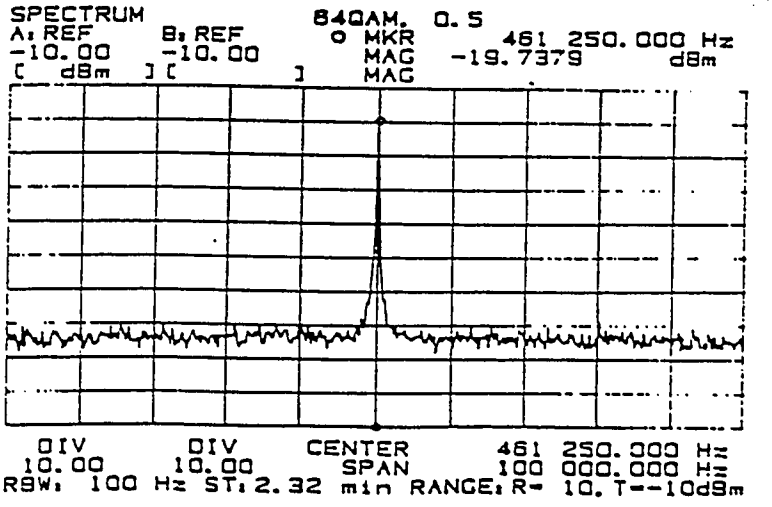

Figure 4.8- Spectrum of the recovered clock for three modulation cases

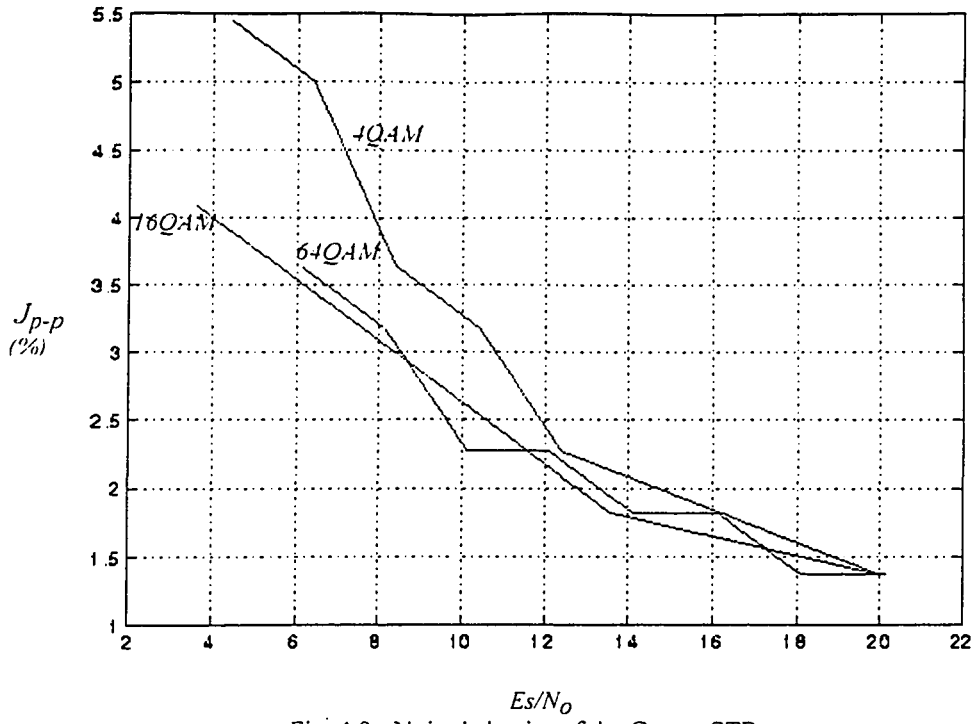

Fig. 4.9 - Noise behavior of the Costas-STR

The improvement in performance can be addressed to the lower bandwidth of the Costas-STR loop, which is mainly controlled by the bandwidth of the loop filter.

4.3.3) Acquisition Time

Figure 4.10 shows the block diagram of the set-up used for acquisition time measurement. A pulse generator switches the transmitter on and off. The STR unit receives the burst data. By receiving each burst, the loop begins to correct the phase and frequency of the VCO. The transient of the VCO control voltage is monitored by the

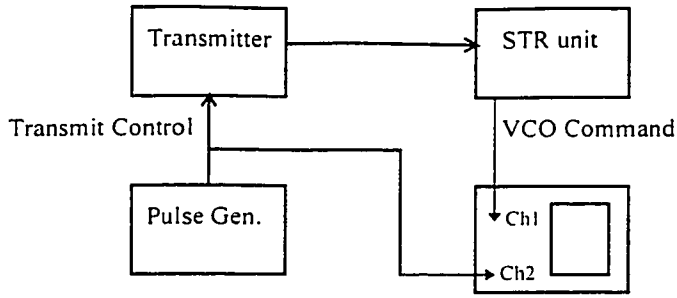

Fig. 4.10 - Lock acquisition time measurement

oscilloscope. The lock acquisition time is measured as the rise time of the VCO command-voltage from 10 to 90 percent of its final value. Table 4.2 shows results of lock acquisition time measurements for different cases of M-PAM signals.

Test Case	*Acquisition Time*
2-,4-,8-PAM	400ms

Table 4.2 - Acquisition time measurement for different case of M-ary signal

As seen, locking process is quite slow and the scheme fails for the burst mode of data transmission. To reduce the acquisition time the loop filter bandwidth should be increased. By increasing the loop filter bandwidth of the implemented unit, the jitter performance is deteriorated resulting in losing lock. The implemented unit was tested for different loop filter bandwidths up to 7 times higher than the primary selected value, however no improvement was observed.

The other parameter which may influence lock acquisition time is the bandwidth of the arm filters $H(f)$. The bandwidths of the filters were changed from 10 to 20 and 40KHz, however it did not improve the lock acquisition time.

4.3.4) Capture Range and Lock Range Measurements

It is required that the clock recovery unit tolerates frequency changes of the transmitter clock due to aging and temperature variation. In such conditions, the system should be able to lock to the transmitter signal and track its frequency variations.

The band of frequencies of the transmitter clock where the STR loop can acquire the lock, is known as the capture range. The lock range is the range of the frequency where the STR loop can maintain lock with the transmitter clock and track its frequency or phase variations.

In Table 4.3, lock acquiring and tracking ability of the loop for different cases are reported. As seen, the 2-PAM case has the widest range of capturing and locking performance. Based on the PLL theory the capture and lock range of a phase locked structure is directly proportional to loop gain. Since the peak to peak amplitudes of the input signals during the test for all the cases were kept fixed to avoid distortion , and the gain of the phase detection function Eq.(4.18) is proportional to $E[a^2]$, the 2-PAM case gives the widest, and 8-PAM the lowest range of lock acquiring and tracking capabilities of the STR loop.

	Capture range (KHz)	*Lock range* (KHz)
2-PAM	$f_u - f_l$=479-450=29	$f_u - f_l \cong$2(535-460)=150 *
4-PAM	$f_u - f_l$=470-454=16	$f_u - f_l$=520-390=130
8-PAM	$f_u - f_l$=467-454=13	$f_u - f_l$=505-404=101

* The lowest frequency of the VCO was 390KHz and still able to lock.

Table 4.3- A summary of lock acquiring and tracking performance of the implemented unit

4.4) Discussion and Summary

The Costas loop structure was introduced for very low jitter symbol timing recovery. It was shown that, the scheme is equivalent to the squarer with prefilter to achieve zero-jitter operation. The following remarks can be made:

- In this scheme, there is no need to any prefiltering. Frequency translation of the baseband signal following by lowpass filtering, provides the same result as the case of ideal prefiltering. The lowpass filter *H(f)* can be designed in a very simple way and it is not required to match to the spectrum of the received signal.
- To achieve very low jitter in the squarer timing recovery, besides employing the prefilter, it is also required to have a very narrow bandpass filter, e.g., a phase locked loop. This implies, for the squarer based scheme, three modules have to be employed namely: the prefilter, squarer and a high performance bandpass filter (PLL). However, for the case of Costas loop STR, there is no need for the prefilter and the phase lock mechanism is already imbedded in the structure.
- It is demonstrated that the scheme can be successfully applied for M-PAM signals with an extremely low jitter, which is an essential requirement for multi-level modulation.

Chapter 5

Conclusion and Suggestion for Further Study

5.1) Summary and Conclusion

It is shown that the proposed conditions by Franks and Bubrowski [5] for zero-jitter operation of the squarer STR for binary signaling can be extended for M-ary PAM (or QAM) signals. These requirements are difficult to meet in practice, and hence, the effectiveness of prefiltering has been questioned [7]. In this work, we investigated the effects of imperfections in both pre-filtering and post-filtering on the jitter performance using analysis, simulation and experiments. It is shown that, although a zero-jitter cannot be achieved due to the imperfections, a good selection of prefiltering can significantly reduce the timing jitter of the recovered clock signal.

By including the prefilter, Q requirement of the bandpass filter can be relaxed. The advantage of having a lower Q is two-fold. First, the complexity and sensitivity of the circuit to misalignment are less. At the same time, it helps to achieve faster lock, which is

another important aspect of the STR schemes. Jitter performance of the squarer with and without prefiltering for M-ary PAM signals is presented.

We also demonstrated that a perfect *prefiltering* of the received *baseband* signal essentially produces an equivalent *double-sided band, suppressed-carrier* (DSB-SC) passband signal centered at the Nyquist frequency (i.e., ½ of the symbol clock frequency). Therefore, the *squarer* actually plays the role of a carrier recovery of the *equivalent* DSB-SC signal and reproduces a carrier tone at *twice* the Nyquist frequency. This observation leads to the introduction of a Costas-loop to replace both the *squarer* and the bandpass *post-filter*. Subsequently, we showed that the required *prefiltering* can be embedded in the Costas-loop lowpass filters. In this approach, the needs for matched highpass pre-filtering and symmetric bandpass post-filtering are eliminated and a very low jitter recovered symbol clock signal can be achieved with a simple Costas-loop. Jitter performance can be enhanced with a narrow lowpass loop filters. Furthermore, the introduced Costas-loop does not employ any non-linear operation, which otherwise could introduce more jitter due to the nonlinear AM-to-PM effects. Analytical and experimental results show that the introduced technique is applicable to both M-ary QAM and PAM signals to achieve a very low jitter performance without any stringent requirement.

5.2) Suggestion for Further Study

- A jitter analysis for the Costas loop timing recovery scheme can be done to investigate the effect of imperfections and noise.

- Current trends of modern communication systems demand fully digital implementation of modem. The proposed Costas scheme could be reviewed and modified for a digital implementation.
- As discussed in the chapter four, the loop has a very slow locking process. Further study to achieve fast acquisition is desired for burst-mode applications. In a digital version, the problem of recovery time might be mitigated to a certain level. The received signal can be sampled and stored in a buffer while waiting for the loop to establish synchronization. This way, an extremely low jitter performance with virtually zero length preamble might be achieved.

BIBLIOGRAPHY

[1] ESTI, Digital broadcasting systems for television, sound and data services; Framing structures, channel coding and modulation for cable systems, ESTI, DE/JTC-DBV-7, 1994.

[2] Yoichi Saito, Yasuhisa Nakamura, 256 QAM Modem for High Capacity Digital Radio System, IEEE Transaction on Communications, VOL. COM-34, No. 8, pp. 799-805, August 1986.

[3] T. Noguchi, Y. Daido, J.A. Nossek, Modulation Techniques for Microwave Digital Radio. IEEE Communication Magazine, VOL. 24, No. 10, pp. 21-30, October 1986.

[4] Yoichi Saito, Shozo Komaki, and Masayoshi Murotani, Feasibilty Considerations of High-Level QAM Multi-Carrier System, IEEE International Conference on Communications, pp. 665-671, May 1984.

[5] L. E. Franks and J. P. Bubrowski, Statistical Properties of Timing Jitter in PAM Timing Recovery Scheme, IEEE Transaction on Communications, VOL. COM-22, No.7, pp. 913-920, July 1974.

[6] Floyd .M. Gardner, Clock and Carrier Synchronization: Pre-filter and Anti-hang-up Investigations, ESA CR-984, European Space Agency, Noordwijk, Netherlands, November 1977.

[7] J.E. Mazo, Jitter Comparison of Tones Generated by Squaring and by Fourth-Power Circuits, The Bell System Technical Journal, VOL. 57, No.5, pp. 1489-1498, May-June 1978.

[8] Patrick R. Trischitta, Eve L. Varma, Jitter in digital transmission systems, Artech House, Norwood 1989.

[9] Floyd .M. Gardner, Phaselock Technique, 2nd Edition, John Wiley, NewYork 1979.

[10] J. J. Stiffler, Theory of Synchronous Communications, Prentice-Hall, Englewood Cliffs, NJ, 1971.

[11] U. Mengali, A Self Bit Synchronizer Matched to the Signal Shape, IEEE Transaction AES-7, pp.686-693, July 1971.

[12] L. E. Franks, Carrier and Bit Synchronization in Data Communication- A Tutorial Review, IEEE Transaction on Communications, VOL. COM-28, No. 8, pp. 1107-1121, August 1980.

[13] W. C. Lindsey, M.K. Simon, Telecommunication Systems Engineering, Prentice-Hall, Englewood Cliffs, NJ, 1973.

[14] M. K. Simon, Nonlinear Analysis of an Absolute Value Type of an Early-Late Gate Bit Synchronizer, IEEE Transaction on Communications, VOL. COM-18, pp. 589-597.

[15] W. C. Lindsey, R. C. Tauseworthe, Digital Data-Transition Tracking Loop, JPL SPS, 37-50, Vol. III, pp. 272-276, Jet Propulsion Laboratory, Pasadena, CA., April 1968.

[16] W. R. Bennett, Statistics of Regenerative Digital Transmission, BSTJ, VOL. 37, pp. 1501-1542, November 1958.

[17] Tho Le-Ngoc and Kamilo Feher, A Digital Approach to Symbol Timing Recovery Systems, IEEE Transaction on Communications, VOL. COM-28, No. 12, December 1980.

[18] Takasaki, Yashitaka, Digital Transmission Design and Jitter Analysis, Boston, Artech House 91.

[19] Yoshitaka Takasaki, Timing Extraction in Baseband Pulse Transmission, IEEE Transaction on Communications, VOL. COM-20, No. 5, pp. 877-884, October 1972.

[20] Floyd .M. Gardner, A BPSK/QPSK Timing-Error Detector for Sampled Receivers, IEEE Transaction on Communications, VOL. COM-34, No. 5, pp. 423-429, May 1986.

[21] I.Frigyes, Z.Szabo, P.Vanyai, Digital Microwave Transmission, Szegedi Nyomda, Hungary 1989.

[22] G. 702, CCITT Yellow Book, Vol. III-3, (Geneva, 1981).

[23] J. J. Baldini, M. W. Hall, R. J. S. Bates, Jitter in Digital Transmission System - Characteristics and Measurement Techniques, IEEE Int. Con. Comm. 1982, pp.658-664.

[24] Rodger E. Ziemer, Roger L. Peterson, Digital Communications and Spread Spectrum Systems. 1st Edition. Macmillan Publishing Company, New York 1985.

[25] Jack K. Holmes. Coherent Spread Spectrum Systems. 1st Edition, John Wiley, NewYork 1982.